Design of Linear Series Elastic Actuators for a Humanoid Robot

Coleman Scott Knabe

Thesis submitted to the Faculty of the
Virginia Polytechnic Institute and State University
in partial fulfillment of the requirements for the degree of

Master of Science
in
Mechanical Engineering

Dennis Hong, Co-chair
Brian Lattimer, Co-chair
Craig Woolsey

5 December 2014
Blacksburg, Virginia

Keywords: Series Elastic Actuator, Hoeken's Linkage, Parallel Actuation, Humanoid Robot

Design of Linear Series Elastic Actuators for a Humanoid Robot

Coleman Scott Knabe

(ABSTRACT)

Series elastic actuators (SEAs) have numerous benefits for force controlled robotic applications. This thesis presents the design and assembly of a set of compact, lightweight, low-friction linear SEAs for the legs of the Tactical Hazardous Operations Robot (THOR). The THOR SEA pairs a ball screw driven linear actuator with a configurable titanium leaf spring. A removable pivot changes the effective cantilever length, setting the compliance to either 372 or 655 kN/m. Unlike typical SEAs which measure actuator load through spring deflection, an in-line axial load cell directly measures actuator forces up to the commandable peak of 2225 N. The continuous operating range of the actuator is computed, along with an evaluation of the range of motion and torque profiles for the parallel hip and ankle joints. With a focus on a large power-to-weight ratio and small packaging size, the THOR SEAs are well-suited for accurate torque control of the parallel joints on the robot.

Linearly actuated joints, especially ones driven through a crank arm, tend to suffer from a loss of mechanical advantage toward the ends of its limited range of motion. To augment the range of motion and mechanical advantage profile on THOR, an inverted Hoeken's linkage straight line mechanism is paired with a linear SEA at the hip and knee pitch joints on the robot. The resulting linkage assembly is capable of delivering nearly constant peak torque of 115 Nm across its 150 degree range of motion. The mechanical advantage profile of the Hoeken's linkage actuator is computed for the nominal case, as well the deviation resulting from maximum deflection of the titanium beam.

This work was supported by ONR through grant N00014-11-1-0074 and by DARPA through grant N65236-12-1-1002.

Acknowledgments

I would like to thank the many people who have helped me reach this momentous achievement. First I must acknowledge my advisors, Professors Dennis Hong and Brian Lattimer, who have helped guide me through the process of my graduate study. Dr. Hong, thank you for recognizing my potential as a RoMeLa graduate student, for providing me with interesting and challenging problems to tackle, for sending me on trips around the world to present and demo the lab's work, and for reminding me to "first work smart, then work hard." Dr. Lattimer, as a late addition to my committee, you impressed me with your ability to comprehend, evaluate, and offer improvements for intricate systems outside your typical area of research. Your guidance while finalizing the scope and structure of my thesis work proved invaluable to my success. Thank you both for the encouragement, positive reinforcement, and appreciation you showed for my hard work and dedication.

To my mother and father, thank you for supporting me throughout the highs and lows of my undergraduate and graduate careers. I attribute much of the success I have had to the lessons and values you have taught me. Thank you for keeping the "when are you actually going to graduate" questions to a minimum, and for consistently considering "I honestly don't know" as an acceptable response. Thank you for always being interested in receiving updates on lab and school work, even if you did not fully understand the technical aspects. Thank you for providing me with a nearly endless supply of Lego, K'NEX, Technic, and Mindstorm sets as a child; these really were the building blocks for my interest in engineering.

To my RoMeLa and TREC lab mates, it has been an excellent experience learning from, and helping to teach, some of the most brilliant engineers and future roboticists I know. From the formal design reviews to the wacky hypothetical brainstorming sessions, the majority of my mechanical design knowledge was gained from the students of these labs. Thank you all for nurturing an inviting, hard-working, exciting, and intellectual lab environment.

I especially would like to recognize everyone who contributed toward the development of the THOR SEAs: Bryce for providing design insights and potential improvements learned from SAFFiR SEA development, and for coordinating the initial THOR design iteration process; Viktor for designing the compliant beam and attachment interface for the actuator, and for assisting in designing and analyzing results of actuator experiments on the test stand; Derek for providing invaluable feedback and direction for our mechanical design approaches, and

for encouraging me to investigate the usage of the Hoeken's linkage on THOR; Mike for developing and tuning the robust joint impedance controller employed on the THOR SEA, for maintaining your patient resolve during my repeated questions and mistakes regarding actuator control, and for your motivation and persistence to make THOR walk as a validation of your whole-body controller as well as my SEA design; Steve for creating the motor slug and power amplifier for the actuators, and for always being vocal when you were sure "there is no way that's going to work"; Jack-Jack for somehow maintaining your composure despite the onslaught of designing, soldering, crimping, and repairing electronics for the robot and test stand; Taylor and numerous others for assisting with machining and post-processing of actuator and robot components; and Joe for teaching me a thing or two about effective leadership strategies and maintaining lab morale through some of its most stressful moments.

To my numerous friends who have come and gone through Blacksburg in my years here at Virginia Tech, I thank you for all the times we shared in this amazing town. To Liz, for always celebrating the days of achievement, as well as supporting me in days of discouragement; to Cory and Dan for always finding a reason for me to get out of lab every few days; to my numerous roommates for always exhibiting a fascination and appreciation of my research; to Charlie, Ingrid, Caitlin, Seth, and Aaron, the late night beers, music, and home cooking were always something to look forward to while writing this. You all are what have made these past few years truly enjoyable.

Thank you.

Contents

List of Figures

List of Tables

Chapter 1

Introduction

Series elastic actuators (SEAs) have several benefits for force controlled robotic applications, including high bandwidth force control, energy storage, and shock tolerance [1], [2], [3], [4], [5], [6], [7]. Several humanoid robotic platforms use linear SEAs for those benefits and because they mimic the biomechanical structure of legged animals [1], [3], [8], [9], [10], [11]. Linear actuators can be placed close to lightweight skeletal bodies while positioning the majority of their mass and volume away from the joint itself.

The original SEAs were designed around ball screw drives with coil springs to provide the elastic element [1], [3], [4]. In the years since, there has been a variety of SEA designs including: rotary actuators [12], [13], [14] and linear actuators [6], [15], [16]; novel design features such as nonlinear stiffness [17], variable stiffness [18], [19], [20], and variable damping [21], [22]; and diverse control approaches [2], [6], [23], [24], [25].

Series elasticity plays a large role in determining the effectiveness of an SEA. Low-elasticity systems are easier to control, but have worse force control performance. High-elasticity systems are the opposite, sporting better performance capabilities at the cost of more difficult control. A few groups have designed compliant mechanisms that have a range of stiffnesses [18], [26], [27]. These mechanisms allow the user to alter the performance of their SEA without manufacturing a new system.

Parallel actuation enables multiple actuators to control the same number of degrees of freedom in a joint. Several legged robotic platforms use parallel SEAs to drive their hip and ankle joints [8], [9], [11]. This actuator configuration moves mass higher up each link, decreasing the overall inertia of the leg. Additionally, two actuators cooperatively pushing on a joint can increase its torque potential compared to each actuator driving its own joint.

1.1 Motivation

Robots are suited to remove humans from dirty, dull, and dangerous situations. Due to the similar form factor to humans, humanoid robots are inherently poised to perform in human-centered environments. Over the years, advancements in robot design, sensor, power, and controls have enabled bipedal robots to walk reliably on uneven and unstructured terrain. There is a large interest in fielding rescue robots to assist humans in dangerous tasks. One of the largest funded efforts toward disaster response robot development is the DARPA Robotics Challenge.

1.1.1 DARPA Robotics Challenge

The DARPA Robotics Challenge (DRC) was introduced in 2012 as a worldwide competition to develop robots capable of assisting humans in responding to natural and man-made disasters. The resulting technologies developed for the DRC will expand the field of robotics and advance the development of autonomous systems that can operate in the hazardous and degraded conditions common in disaster zones.

Some of the original DRC tasks included a rough terrain walking course, entering and driving a vehicle, opening doors, climbing stairs, turning valves, and using tools. DARPA does not regulate the form factor of the robot used for the competition, but with its previous experience in bipedal locomotion, the Virginia Tech team determined that a humanoid robot was the best design for interacting with a human-centered environment. These tasks drove the range of motion and torque requirements for the team's robot entry for the DRC.

1.1.2 SAFFiR

SAFFiR, pictured in Fig. 1.1, is the Shipboard Autonomous Fire Fighting Robot developed for the Navy's SAFFiR project. This 12-DOF lower body features linear SEAs arranged in both serial and parallel configurations and uses a hybrid position controlled walking strategy with compliant force controlled ankles [28]. This walking strategy enables the robot to traverse unstructured and unstable terrain.

The actuator described in this thesis is an evolutionary improvement upon the SAFFiR SEA, shown in Figure 1.2. The SAFFiR linear SEA is designed around a ball screw, but its configurable compliant spring is isolated from the linear actuator [15]. This packaging allows for the redesign of either subsystem without impacting the other. Unlike actuators which estimate actuator force through spring deflection, an in-line load cell measures actuator force directly. SAFFiR utilizes force control in the parallel ankle joint; however, the robot has a limited range of motion and torque which render it incapable of performing many of the DRC tasks. Many design concepts tested on SAFFiR, including parallel actuation and force

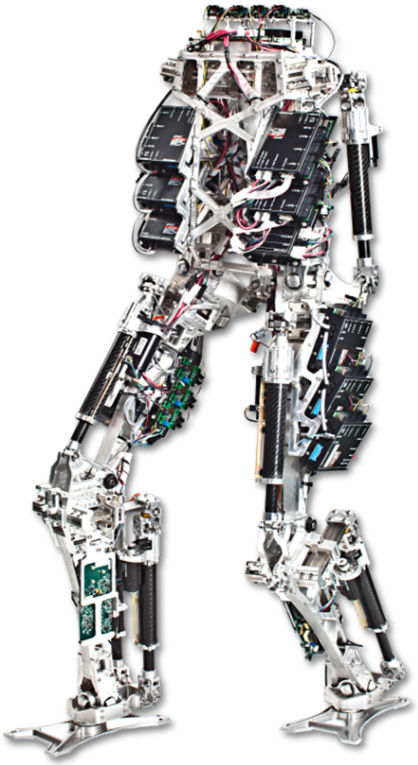

Figure 1.1: Shipboard Autonomous Fire Fighting Robot (SAFFiR), from website http://www.maxonmotorusa.wordpress.com/tag/romela/, used with permission of Maxon Precision Motor, Inc., 2014.

control, were used as a basis for the design of the new robot entry to the DRC.

Figure 1.2: Rendering of the linear SEA used on SAFFiR, from "Design and Measurement Error Analysis of a Low-Friction Lightweight Linear SEA," used with permission of Bryce Lee, 2014.

1.1.3 THOR

The Tactical Hazardous Operations Robot (THOR), seen in Fig. 1.3, is a 1.78 m tall, 60 kg humanoid robot and is Virginia Tech's entry into the DRC. It was designed to carry either the computer and batteries needed to enable untethered teleoperation for 20 minutes, or three computers to handle the computational load of autonomous operation of the robot. With a multi-spectral sensor array in the head, custom underactuated hands, and a lower body with a human-like range of motion, THOR is poised to compete as a disaster response humanoid.

The lower body features twelve linear SEAs arranged in different configurations to achieve a range of motion comparable to other DRC competitors. THOR features three similar versions of the SEA: two driving each ankle roll/pitch joint through a load bearing carbon fiber tube, two for the knee and hip pitch joints driven by a mechanical linkage connected to the output of the ball screw, and a more compact carbon fiber version for the hip roll/yaw joints [9]. The actuators spanning the hip and ankle joints are in a parallel configuration, in which two actuators cooperatively control two intersecting, orthogonal joint axes. The actuators attach through custom universal joints to the structure of THOR and to the compliant titanium leaf springs. Similar to the SAFFiR SEA design, the configurable compliant beam is an independent assembly from the actuator.

Design requirements for THOR were derived based on the DRC task descriptions, simulations, and testing from SAFFiR. The range of motion (ROM) specifications are listed in Table 1.1. The proposed robot frame required the actuators maintain a small minimum length while featuring a large travel length. Based on an estimated model and kinematic arrangement of a full sized humanoid robot, torque requirements were derived which required the SEAs be capable of delivering at least 2000 N of peak force. These requirements drove the design of the THOR SEA. To achieve the extended range of motion in the serial hip pitch and knee joints, an inverted straight line mechanism is paired with the linear SEAs to

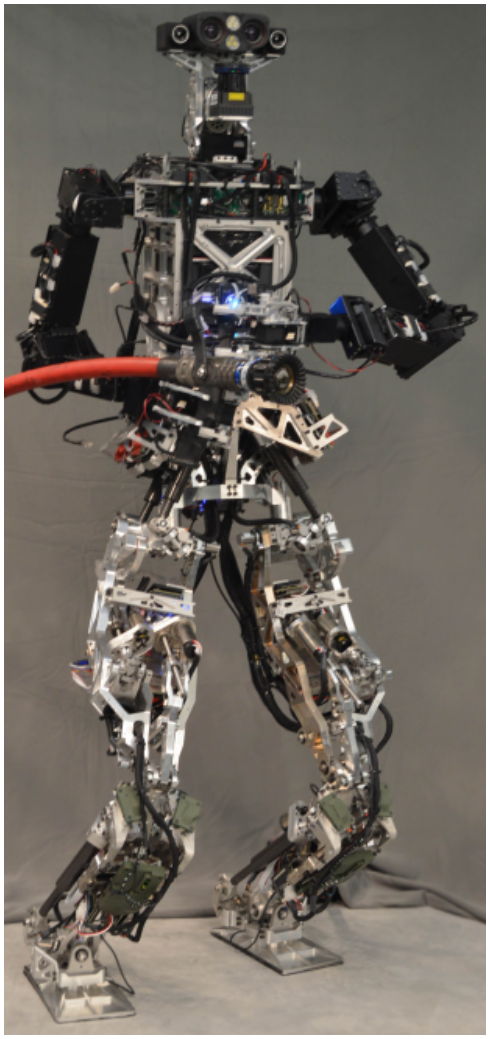

Figure 1.3: Tactical Hazardous Operations Robot (THOR), photographed by and used with permission of Eric Hahn, 2014.

address the mechanical advantage limitations of linearly actuated joints. Further details on the design of THOR can be read in [29].

Table 1.1: THOR Range of Motion

Joint Axis	Minimum	Maximum
Hip Roll	–30	45
Hip Pitch	–120	30
Hip Yaw	–20	45
Knee Pitch	0	135
Ankle Roll	–30	30
Ankle Pitch	–55	35

1.2 Contributions

A set of compact linear series elastic actuators have been designed and manufactured to drive the lower body of a full sized humanoid robot. By maintaining a small actuator length and utilizing a mix of parallel and serial joint arrangements, the robot achieves a human-like range of motion. Since linearly driven joints suffer from range of motion limitations, an inverted Hoeken's linkage straight line mechanism is paired with the linear actuator to increase the joint range of motion and mechanical advantage of the knee and hip pitch joints. The low backlash, high-efficiency SEA design is a critical subsystem enabling THOR's whole-body controller to reliably walk on unstructured and shifting terrain.

1.3 Thesis Organization

This thesis encompasses the design of the custom series elastic actuators for THOR. Chapter 2 details the mechanical and electrical design of the THOR linear SEA, including an analysis of the peak torque of each joint on the robot. Chapter 3 overviews the design of the inverted Hoeken's linkage mechanism used in the hip pitch and knee joints to augment the range of motion and mechanical advantage limitations of linearly actuated joints. Chapter 4 presents a summary of work, recommends improvements for future actuator designs, and proposes future research topics pertaining to the THOR SEA.

Chapter 2

Linear Series Elastic Actuator

2.1 Introduction

Series elastic actuators (SEAs), unlike conventional rigid actuators, are characterized by a spring placed in series with an actuator's output. The original SEAs were designed around ball screw drives with coil springs to provide the elastic element [1], [2], [3], [4], [5], [6]. These SEAs are self-contained packages that are well designed for high bandwidth force control. By building around an efficient ball screw the overall friction in the system is decreased, allowing the actuator to command small forces without the interference of Coulomb friction.

The design decision was made for THOR to utilize linear actuators because they can be mounted in close proximity to a lightweight skeletal structure, offer an easy means of achieving parallel joint actuation schemes, and are an elegant solution to realize bio-inspired legged locomotion. A typical linear SEA consists of a motor to generate mechanical power, a gear reduction to increase the available motor torque, a transmission to transfer the load to an actuated joint, and a compliant element to enable impact resistance and force sensing. Existing SEAs select and configure these components in various ways resulting in trade-offs affecting cost, complexity, size, weight, backdrivability, unpowered impedance, shock tolerance, power output, and efficiency.

Force-controllable hydraulic actuators, such as those developed at the MIT Leg Laboratory [30] or used on SARCOS [31], achieve high power-to-weight and power-to-volume ratios, but suffer from system complexity, difficulty in backdriving, high impedance due to seal friction and low compressibility of the hydraulic fluid, and nonlinear control behaviors. While there are SEAs designed around inexpensive servo motors [32], [33], many high-performance electric SEAs use brushless direct current (BLDC) motors for their efficiency, power density, load capacity, and relative ease of control [1], [6], [34]. Furthermore, Taylor in [35] uses two BLDC motors to drive the gear reduction, achieving the same output torque with twice

the speed of a single motor.

Numerous approaches for speed reduction have been used for linear SEAs. [1] and [36] use planetary gearheads which are relatively inexpensive and efficient, yet can become heavy and bulky to achieve high gear ratios. [3] and [4] connect the BLDC motor output directly to a ball screw drive to serve as the only speed reduction. Numerous linear SEAs employ a timing belt pulley reduction between the motor and primary transmission [6], [15], [37], [38].

The primary drivetrain is also a source of variety in SEA designs. The majority of linear SEAs are built around precision ball screw drives due to their low friction and backlash, high efficiency and gear reductions, tolerance to impact load, and ability to backdrive. To drive a rotary joint, some SEA designs connect the ball screw output to a cable transmission to remotely drive the joint [37], [38], [39], [40], which face issues of cable stretch, creep, tensioning, wear, and temperature sensitivity. Other designs remove the need for a cable transmission by directly driving the joint through a crank arm [2], [15], [38]. The linear SEAs on Valkyrie utilize roller screws as the primary transmission [34]. There are also linear actuators centered around lead screws [36], [41], [42]. These actuators have more friction and backlash in the system, but are lower in cost and lighter weight. Depending on the application, this may be a more important design consideration.

While there is a plethora of compliant element implementations for rotary SEAs, spring selection for linear actuators is more limited. The majority of linear SEAs use one or more compression die springs as a low-cost, reliable, and relatively linear source of compliance [1], [4], [6], [36], [37]. Actuator force within these actuators is estimated by measuring spring deflection through potentiometers, converting the force control problem to a position control problem. Hollander uses a unique Jack Spring^{TM} mechanism in [43] which adjusts the number of active coils of the helical spring, coupling stiffness and displacement of the actuator.

Conversely, the SAFFiR SEA uses a cantilevered titanium leaf spring connected to the actuator through a universal joint which loads the spring in bending, while a load cell mounted in-line with the actuator directly measures commanded force [15]. An adjustable pivot mounted along the leaf spring changes the effective length of the cantilever, allowing for configurable compliance [26]. The universal joints at each end of the actuator serve as a simple means of attachment to a robotic frame and provide the degrees of freedom necessary to enable parallel actuation of robotic joints. Unlike many linear SEAs which rely on linear guides to constrain ball nut rotation, the use of universal joints reduces design complexity, weight, and overall friction of the actuator while properly constraining the ball screw assembly for effective force transmission.

The actuators designed for THOR are an evolutionary improvement upon the SAFFiR SEAs described in [15]. The fundamental concept of pairing a titanium leaf spring with a ball screw driven actuator remains the same; however, several redesigned parts and key reconfigurations drastically improve the performance and packaging size over the previous

SEA. The arrangement of each joint on THOR, illustrated in Fig. 2.1, also changed from SAFFiR: the hip roll/yaw and ankle roll/pitch joints are driven by two linear SEAs in a parallel configuration while the knee and hip pitch joints are driven serially by SEAs paired with inverted straight line mechanisms to increase the joint range of motion.

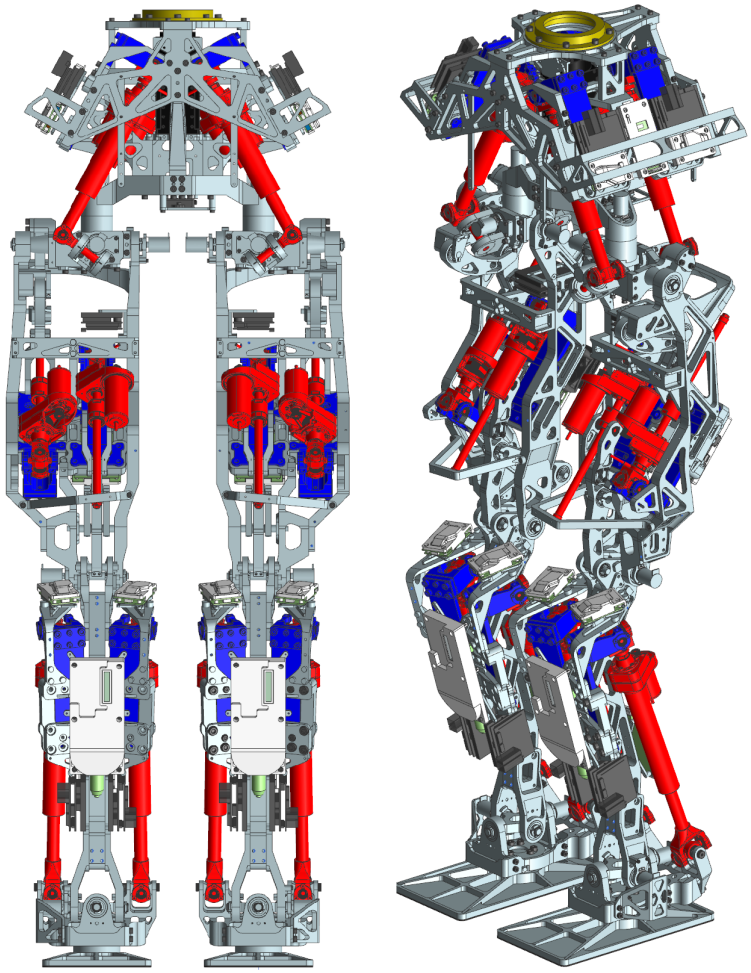

Figure 2.1: Rendering of THOR lower body, highlighting the actuators in red and the compliant elements in blue.

This chapter details the design and expected performance of the THOR SEA. The first section details the key actuator subsystem designs which allowed the actuator to meet stiff packaging and load requirements. The next section overviews the electrical design of the actuator, and the final section discusses the actuator specifications and peak joint torques available on the robot.

2.2 Mechanical Design

A rendering of the THOR SEA used on the parallel hip roll/yaw joint is shown in Fig. 2.2. A custom precision-ground ball screw is positioned at the center of the assembly and is connected to a brushless DC (BLDC) motor through a timing pulley reduction. The transmission housing contains compact pairs of radial and thrust bearings sandwiched around the drive pulley to handle the large forces between the ball screw and the housing. The universal joints on both ends of the actuator ensure it is loaded as a two-force member and also serve as connection points between the actuator and the robot structure. Furthermore, there is no need for a linear guide to restrict unwanted rotation of the ball nut, as the universal joints constrain this rotation instead.

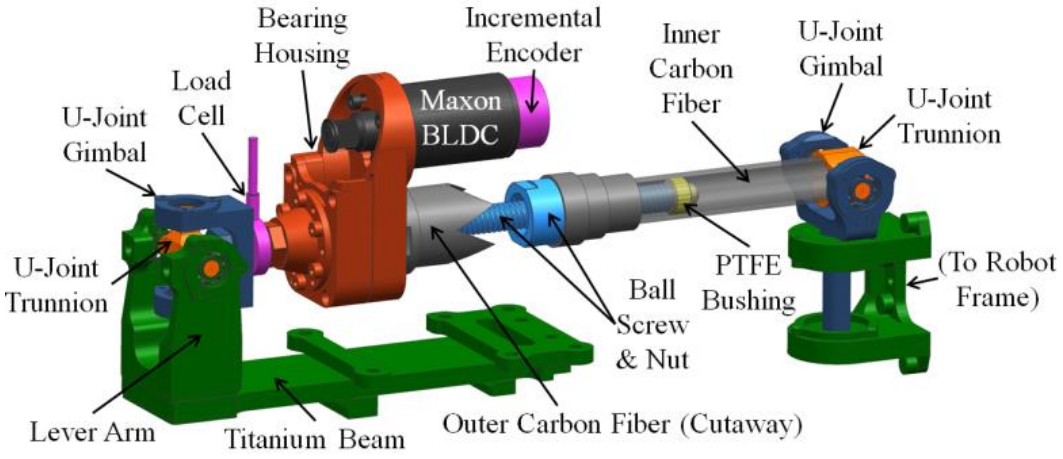

Figure 2.2: Rendering of the THOR hip SEA.

A load bearing carbon fiber tube transmits the force from the ball nut to the universal joint at the bottom of the actuator. A low friction PTFE bushing mounted on radial bearings at the end of the ball screw contacts the inner surface of the carbon fiber tube to maintain proper axial alignment with the ball nut for load transmission. A non-structural outer carbon fiber tube shields the ball screw assembly from damaging debris. Similar to the SAFFiR actuator, the THOR SEA incorporates a tension/compression load cell for direct force sensing rather than estimating force through spring deflection. The compliant element is a titanium cantilevered beam mounted parallel to the actuator and connected through a lever arm to load the beam in nearly pure bending. Each motor has a built-in incremental encoder to measure actuator length, while an absolute optical encoder is located at each joint axis on the robot to measure joint angle and to compensate for the effects cantilever deflection has on force control.

A comparison of the SAFFiR and THOR hip SEAs can be found in Table 2.1. One important measure of a linear actuator's packing size is its fixed length. The fixed length is defined as the length of an actuator with zero-stroke, or the minimum length minus its stroke, which

accounts for all the components that are integral to the actuator's function. A shorter fixed length is beneficial for packaging the actuator within the robot body, especially at joints using parallel actuation. To realize a shorter fixed length, the belt transmission and bearing housing were redesigned to be more compact. Using the same 100 W Maxon EC4-pole–30 motors as the SAFFiR SEAs with a larger 3:1 pulley ratio and a more shallow 2 mm pitch THK precision ground ball screw, the peak force was increased from 1,000 N to 2,225 N and the continuous force more than doubled from 300 N to 685 N. Kinematic arrangement of the actuators on the robot account for the reduced actuator speed, and is sufficient for bipedal locomotion.

Table 2.1: Comparison of the hip SEAs for SAFFiR and THOR

SEA Characteristic	SAFFiR	THOR
Weight (Actuator Only) (kg)	0.653	0.726
Weight (Full SEA) (kg)	0.816	0.938
Maximum Speed (m/s)	0.35	0.198
Stroke (m)	0.110	0.085
Fixed Length (m)	0.153	0.111
Continuous Force (N)	300	685
Peak Force (N)	1,000	2,225
Spring Constant (kN/m)	145 – 512	372 or 655
Ball Screw Lead (mm)	3.175	2.0
Pulley reduction	2.5:1	3:1

Through the modular design of actuator subcomponents, numerous actuator configurations can be achieved with fewer individual parts. Fig. 2.3 shows a rendering of the three configurations of actuators used on the left leg of THOR. The remainder of the actuators for the lower body are variations of these three actuators. Reconfiguration of the titanium beam loading scheme from bending to moment loading (from perpendicular to parallel to the actuator) enables the compliant member to handle the increased actuator forces without failure from stress. This rearrangement also greatly reduced the actuator fixed length and packaging space by removing space from the travel axis typically required for spring deflection. Another critical design change was to reduce the size of each universal joint, creating smaller packages to achieve only the minimum angle range required at each joint. Each of the THOR SEA subsystems are detailed in this section, highlighting the design improvements over the SAFFiR SEA.

2.2.1 Bearing and Transmission Housing

The subassembly with the greatest potential for size reduction from the SAFFiR SEA was the bearing and transmission housing, shown in Fig. 2.4. Much of its design was consequent on the bearings chosen and their arrangement within the housing. The largest bearing that

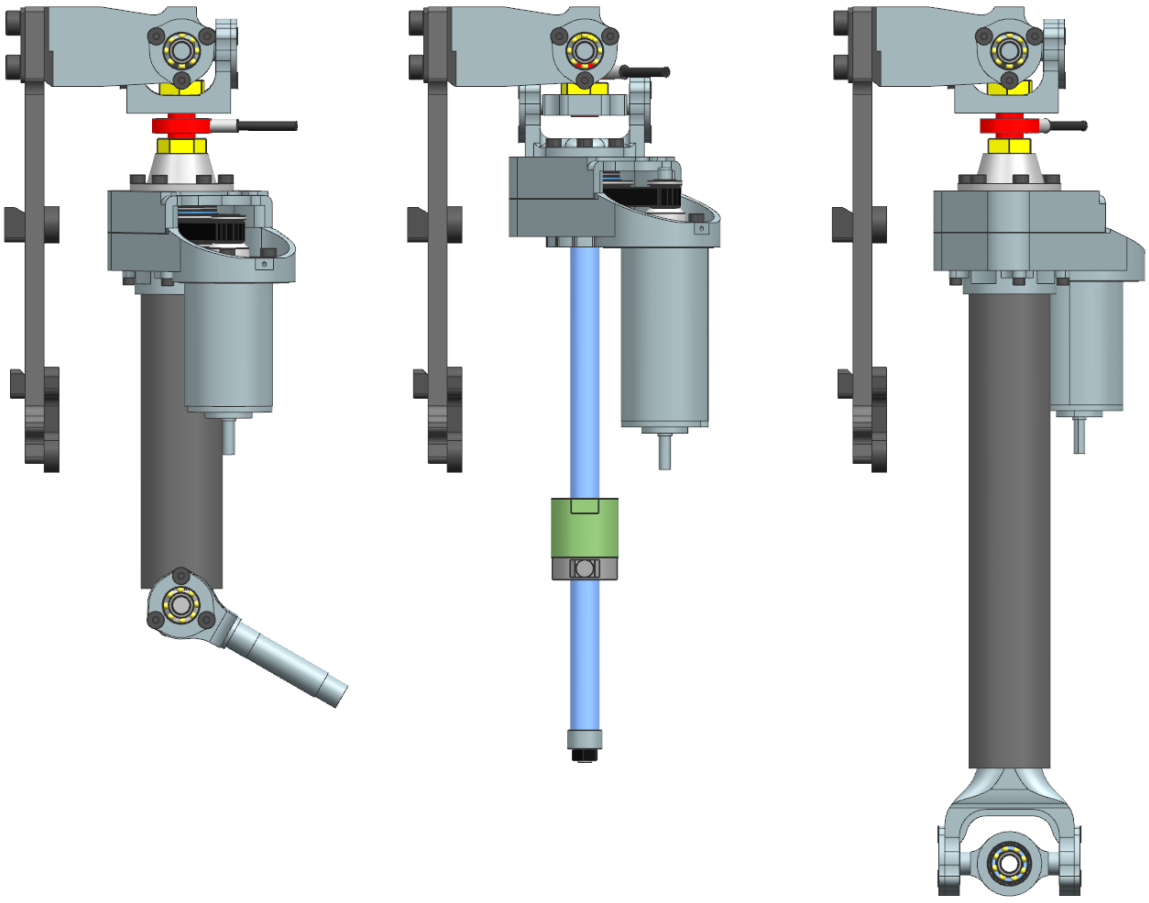

Figure 2.3: Rendering of actuators used on the lower body of THOR. From left to right: hip roll/yaw, knee pitch, and ankle pitch/roll actuators.

the selected ball screw could support was a 7 mm bore: a non-standard size which greatly reduced bearing availability. While angular contact bearings can support a greater axial load than other radial bearings, none were available with a 7 mm bore than could support a 2,225 N axial load. Instead, as listed in Table 2.2, the THOR actuator utilizes a pair of roller thrust bearings to support the high axial load and a pair of deep groove bearings to support small radial tipping loads. A design was chosen, shown in Fig. 2.4, that sandwiches the drive pulley between the two pairs of bearings to reduce the moment load on each bearing and to provide double support for the ball screw while maintaining a compact profile.

Table 2.2: Bearings used in THOR SEA bearing and transmission housing

Bearing Type	Bearing	Dimensions (mm)	Static Load Rating (N)	Dynamic Load Rating (N)
Deep Groove Radial	SMR147C-Y	7x14x3.5	510	1177
Needle Roller Thrust	NTB1024	10x24x2	15000	23900

The drive pulley is aligned to the shaft using bushings press fit into the pulley counterbore. The bushings rest against the inner race of the radial bearings, which are tightened between the ball screw and the retaining nut. A torque wrench is used to tighten the nut to three times the motor stall torque, and friction at the contact surfaces of the bushings constrains the pulley onto the ball screw and prevents slipping. The thrust bearings contact the face of the pulley and are preloaded against the upper and lower housings using shims to eliminate axial backlash. A locational transition fit is used at the contact between the radial bearings and the upper and lower housings to ensure the bearings support no axial loads yet provide an accurate locating surface for the ball screw assembly.

The compression load path, shown in yellow, travels from the ball screw, to the inner race of the radial bearing, to the first bushing, through the pulley, to the upper thrust bearing, and into the upper housing to the load cell. The tension load path, shown in red, is a bit more involved: the load path travels up the ball screw, pulling down on the nut, to the inner race of the upper radial bearing, to the bushing and the pulley, through the thrust bearing to handle the axial load to the lower housing. The load then transfers to the upper housing and housing interface through bolts, then to the load cell. It is important to note that in neither case does the load transfer from the inner race of the radial bearings to the outer race; doing so would destroy the bearings at high load.

The resulting bearing housing constrains the pulley and ball screw as well as eliminates axial and radial backlash within a smaller package than present on the SAFFiR SEA. Furthermore, it provides an interface to the upper universal joint, aligns and fastens the protective outer carbon fiber tube, and contains the belt tensioning motor mount shown in Fig. 2.5.

The motor mount is used to tension the timing belt during installation, and provides a

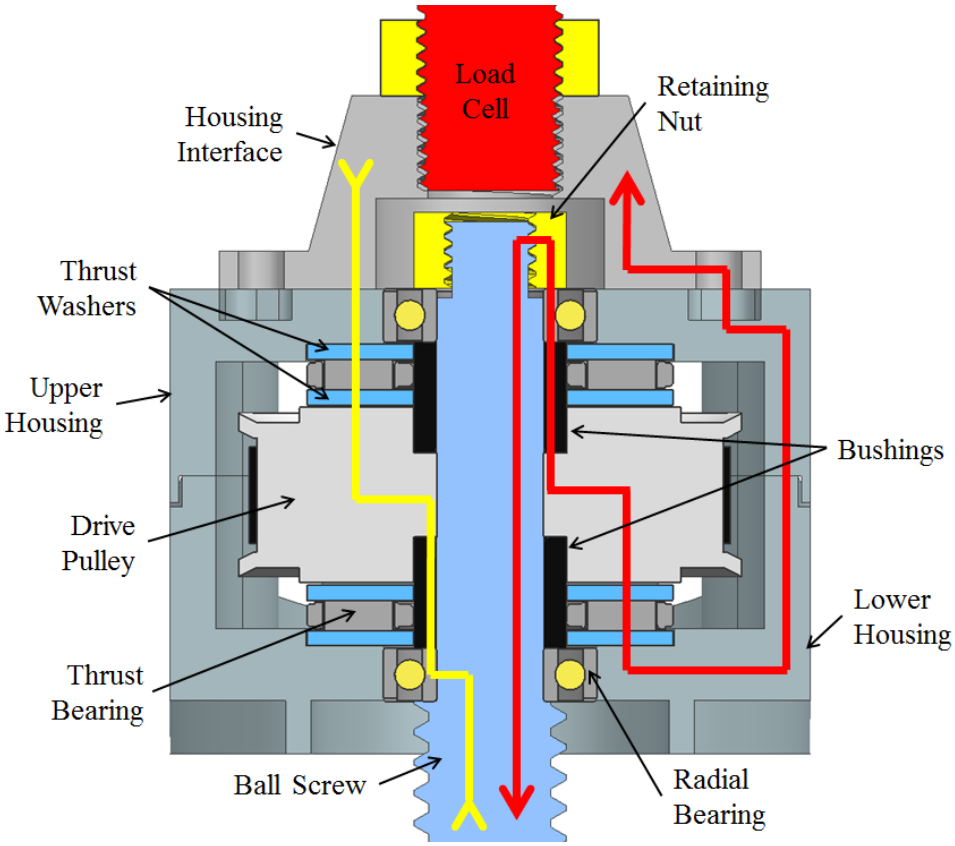

Figure 2.4: Cutaway view of bearing housing, showing the compression and tension load paths. Each load path is symmetrical.

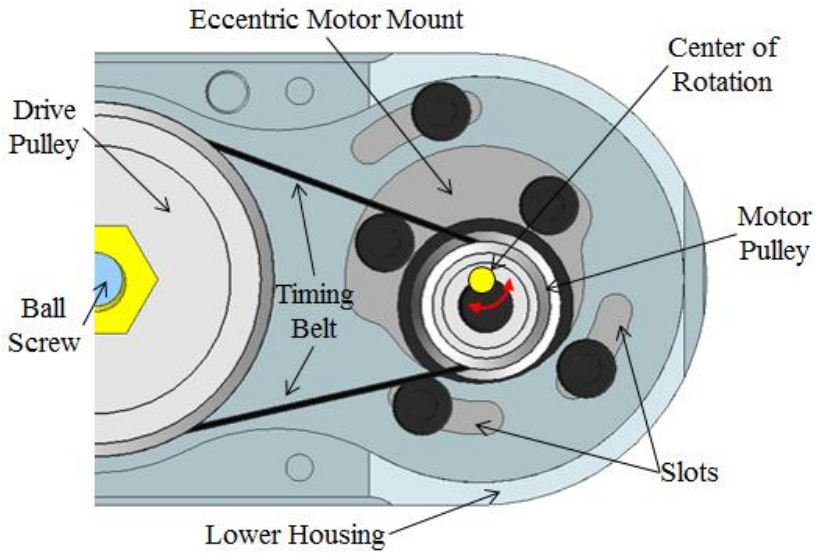

Figure 2.5: Eccentric motor mount for belt tensioning (top view of bearing housing).

rigid means of maintaining tension throughout operation. The motor mounts eccentrically underneath the lower housing and is secured to the actuator housing through three outer bolts. The bolts are mounted through slits in the lower housing and allows the motor mount to rotate through a limited angle range prior to tightening. Rotating the motor clockwise towards the ball screw allows for the belt to slip over the motor pulley during installation, while rotating counter-clockwise away from the ball screw applies appropriate belt tension for operation. This attachment method is a significant improvement over the SAFFiR actuator since it is easy for one person to adjust and set belt tension, and it provides a more rigid structure for both the motor mount and the lower actuator housing. Additionally, the slots are spaced to support a range of pulley reduction ratios in this assembly, allowing easy adjustment of the trade-off between peak force and speed of the actuator. Due to extremely tight packaging constraints, there is a mirrored version of the actuator housing which slightly relocates the motor to avoid interferences with the robot frame.

At the top of the housing is the integrated axial load cell. The Futek LCM200 is attached directly into the housing interface, not split across the universal joint trunnions like the SAFFiR SEA. Though this direct interface increases the fixed length of the actuator, it maintains load cell alignment with the actuator at all times. This design eliminates bending loads on the load cell which can distort measurements and eventually damage or destroy the sensor.

Furthermore, the angle between the bearing housing and the upper universal joint needed to be set accurately to meet packaging requirements on THOR and prevent physical interferences with the body structure over the full joint ranges of motion. This was accomplished through the use of an alignment jig during attachment of the load cell to the housing interface, as shown in Fig. 2.6. The jig accommodates angles at 5 ^{o} increments accomplished through rotation of the threaded load cell and housing connector, allowing the length of the interface to be set to within 0.1 mm for any required housing angle. The jig also constrains the universal joint such that damaging torsional and bending loads do not pass through the load cell while tightening the lock nuts.

2.2.2 Load Bearing Tube

Loads are transmitted from the ball nut to the lower universal joint through the inner carbon fiber tube. Each tube is manufactured on precision ground mandrills for a smooth, toleranced interior diameter. They are then milled to length to maintain a straight and parallel cut and to prevent splintering of the fibers. The ends fit within plug adapters for the ball nut and the lower trunnion, and are epoxied in place after using aluminum etching compound for stronger adhesion. Custom epoxy jigs, shown in Fig. 2.7, were created to ensure proper alignment of the tubes while curing.

To prevent tipping of the ball nut and maintain proper alignment on the ball screw, a low-friction PTFE bushing was installed on the end of the ball screw. As shown in Fig. 2.8 the

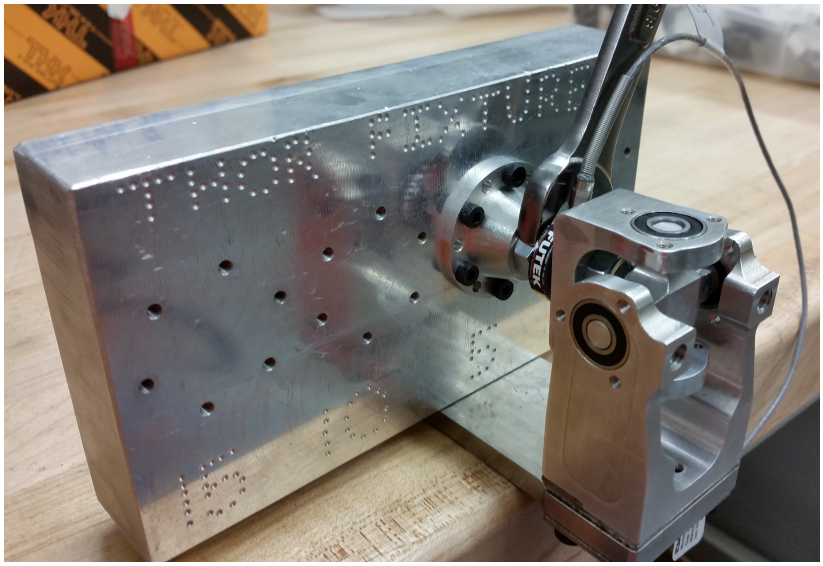

Figure 2.6: Custom jig used to set the alignment angle of the motor housings and load cell cables within the upper universal joint.

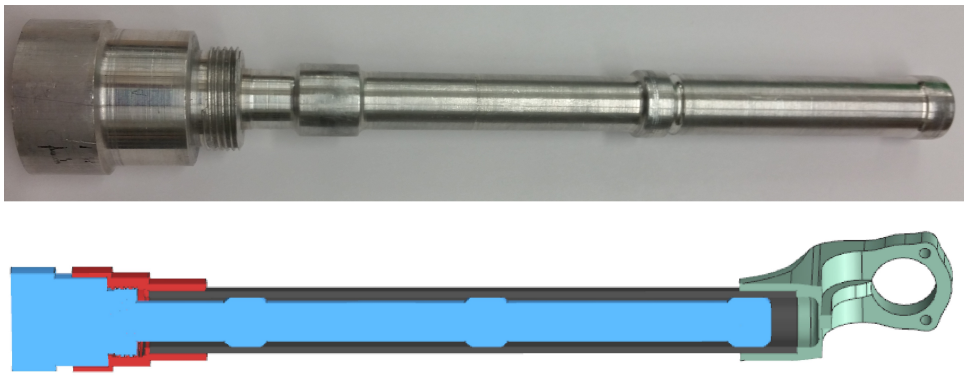

Figure 2.7: Custom epoxy jigs used to align the inner carbon fiber tube assemblies while curing, and a section view showing how the jig constrains each part.

bushing is mounted on two small radial bearings to allow free rotation, while it contacts the inner surface of the carbon fiber tube. Careful design of the end plug adapters on the carbon fiber allow the bushing to travel the entire length of the actuator throw without encountering interferences.

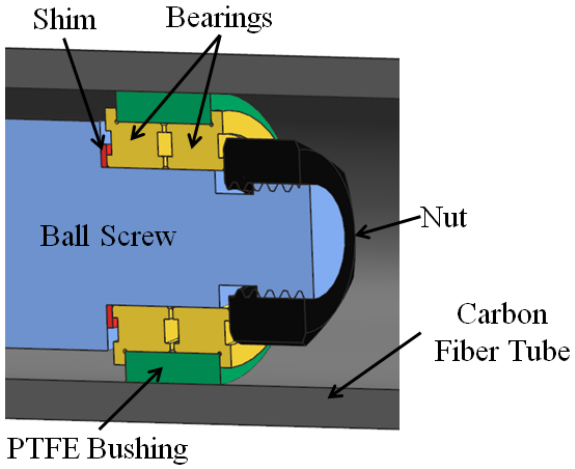

Figure 2.8: Section view of anti-tipping PTFE bushing attached to the end of the ball screw.

2.2.3 Universal Joints

Another portion of the actuator that has a profound effect on the fixed length, the universal joints at each end of the actuator, serve to attach the actuator to the robot frame and constrain the actuator as an axial tension/compression two-force member. The parallel actuation configuration on THOR would not be possible without the use of universal joints at each end of the SEA. The packaging size of the universal joint is highly dependent on the required operating angles of its axes. THOR uses a variety of universal joints, shown in Fig. 2.9, each with varying lengths and configurations suitable for their operating angle ranges.

The universal joint design occurred simultaneously with the actuator end placement on the robot frame because each impacted the other. Moving the actuator ends modified the required universal joint range of motion, which, in turn, changed the attainable fixed length of the actuator. Using the final kinematic arrangement of the THOR actuators, the final range of motion of the roll and pitch axes for each universal joint was determined over its respective joint space, as described in [29].

Overall Upper Universal Joint

The upper universal joint connects the housing of the actuator to the compliant spring. In an effort to reduce the number of unique parts used on THOR, a single upper universal joint,

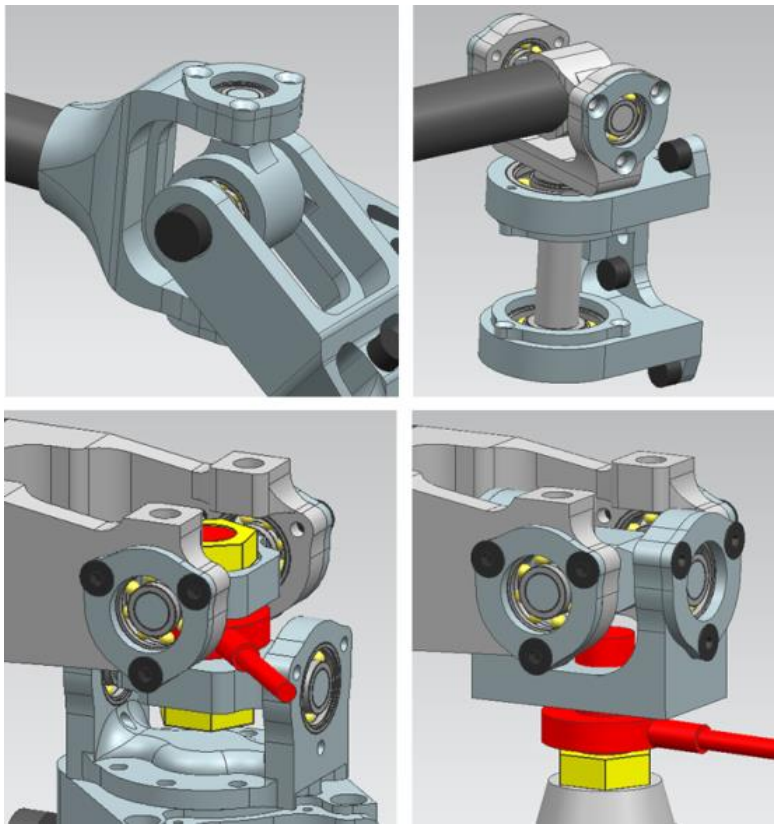

Figure 2.9: Universal joint designs. From upper left to lower right: lower ankle, lower hip, knee, universal upper.

shown in Fig. 2.10, was created which satisfies the angle requirements for each actuator location. The angle requirements collected in Table 2.3 were chosen from the minimum and maximum pitch-roll pair present at the corners of the robot joint space. The upper universal joint follows a traditional universal joint configuration using two gimbals connected by a trunnion with two orthogonal intersecting axes. The pitch axis is defined as the axis of the universal joint attached to the robot structure, and the roll axis is the secondary axis attached to the actuator. Because of the symmetry of THOR, the roll measurement that drove the universal joint design is the larger in magnitude of the minimum and maximum.

Figure 2.10: Upper universal joint in the upper ankle actuator.

Table 2.3: Upper universal joint range of motion requirements in degrees

Universal Joint Location	Min. Pitch	Max. Pitch	Min. Roll	Max. Roll
Front Hip	–3.0	12.6	–7.3	6.4
Back Hip	–4.9	3.7	–14.8	4.0
Ankles	–1.9	3.2	–8.1	2.3
Overall	–4.9	12.6	–14.8	6.4

Interferences between the input and output gimbal are dependent on the operating angle of the universal joint and gimbal height. The shapes of the gimbals were dictated by the bearings selected to handle the peak actuator loads as well as the 50.0 mm lever arm required between the bearing axis and the compliant beam. The trunnion was shaped to withstand the loads of the actuator while not inhibiting assembly. The trunnion is slightly asymmetric with one arm longer than the others. This design allowed for easy assembly of the joint.

Fig. 2.11 shows the maximum achievable universal joint roll angle for a given pitch angle and gimbal height. The data were generated using a preliminary CAD model by varying the height from the bottom of the roll gimbal to its bearing axis and recording the roll angle at which interference occurs. The final gimbal height of 18mm was chosen for the upper

universal joint because it was the minimum length which exceeded the angle requirements of all the universal joints.

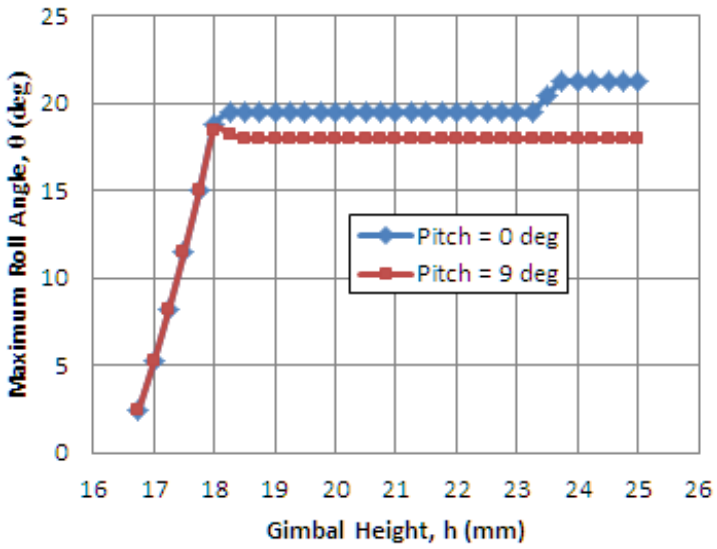

Figure 2.11: Achievable upper universal joint range of motion for a range of gimbal heights.

The same upper universal joint is used to attach the hip roll/yaw and ankle roll/pitch actuators to the compliant spring. Slightly modified versions of the universal joint are used to connect the hip pitch and knee actuators to their respective compliant springs. These joints utilize the Hoeken's linkage mechanisms to obtain a large range of motion with a consistent mechanical advantage. The hip pitch and knee actuators were originally designed with only pin joints at their tops, but testing revealed the need for universal joints to account for manufacturing and assembly tolerance stack up which applied bending loads to the axial load cell causing large errors in the force readings. To reduce the number of remanufactured parts, only the upper universal joints were redesigned instead of the whole thigh structure. The hip pitch actuator, therefore, uses a slightly shorter version of the upper universal joint gimbal than the other hip actuators. This reduces the roll range of motion for that actuator, which is only needed to account for manufacturing and assembly errors of the Hoeken's linkage. The knee pitch actuator, however, uses a completely different trunnion from the other upper universal joints.

Upper Knee Universal Joint

Due to packaging constraints during the universal joint redesign, the knee required a universal joint with smaller packaging than the overall universal joint to avoid a reduced knee range of motion. To accomplish this the knee universal joint, shown in Fig. 2.12, sandwiches the load cell between the two axes of a disjointed trunnion. Negligible displacement of the roll axis maintains alignment of the load cell and ensures proper force readings. As shown in Fig.

2.13, the redesigned trunnion resulted in a 24% length reduction compared to the overall universal joint, with an option to reduce the length even further by reversing the order of the nut and trunnion on the load cell.

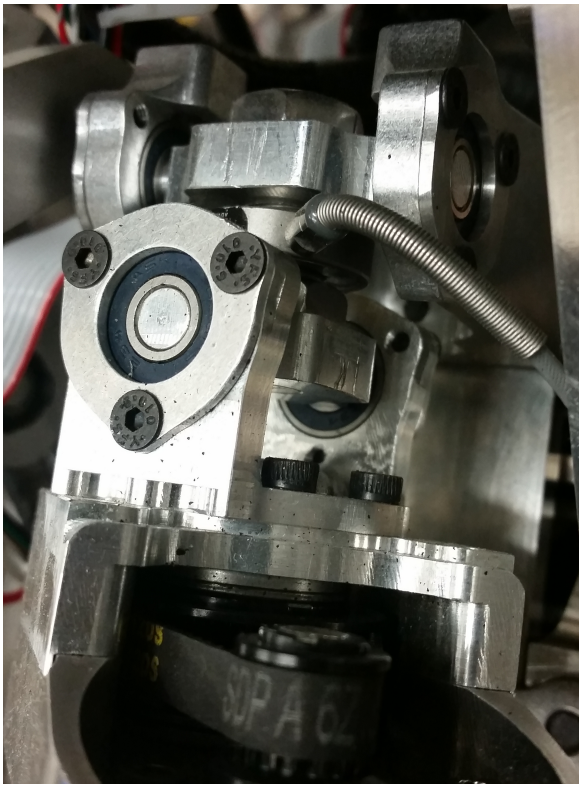

Figure 2.12: Upper knee universal joint installed on THOR.

Lower Hip Universal Joint

The universal joint that connects the hip to the coxa is shaped in an unconventional style. This universal joint has a large range of motion requirement because it is located close to the hip joint [9]. As seen in Table 2.4, the required roll range of motion for this joint is extremely biased and significantly larger than the needed pitch range of motion. The asymmetry in the joint range of motion was motivation to use a non-traditional trunnion design.

Table 2.4: Lower hip universal joint range of motion requirements in degrees

Universal Joint Location	Min. Roll	Max. Roll	Min. Pitch	Max. Pitch
Front Hip	–61.6	22.5	–17.5	6.1
Back Hip	–67.2	27.0	–10.1	7.5

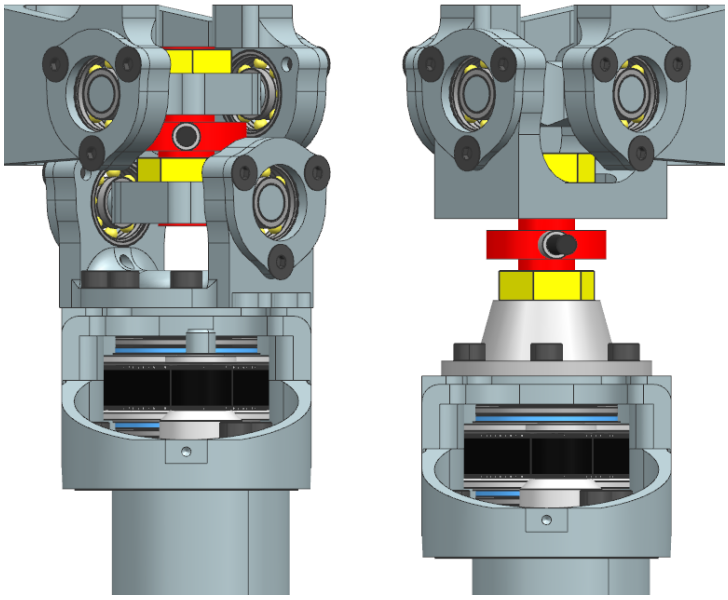

Figure 2.13: Upper knee universal joint (left) compared to the overall upper universal joint (right). Length comparison from the universal joint to top of housing: 47.5 mm and 36 mm.

The roll range of motion would be difficult to achieve with a traditional universal joint design. Additionally, these joints are attached to the outside of the coxa in the middle of the hip joint. It was imperative that the joints not occupy a large volume so they would not interfere with the robot frame over the leg range of motion. A number of trunnion designs were tested before settling on the hybrid gimbal/trunnion design with a wishbone shape. This shape reduced the outward profile of each universal joint while providing a larger region of unimpeded roll motion. The joint attached to the coxa is shown in Fig. 2.14.

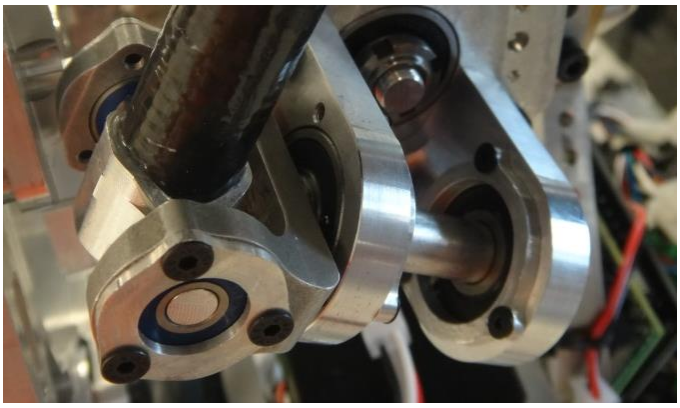

Figure 2.14: Lower universal joint for the hip actuators.

Though this universal joint design allows for the necessary range of motion, it has its

detriments. First, one of the axes of the trunnion is placed in single support. This required the use of larger bearings to support the radial loads.

This configuration for the cross gimbal presents a new failure mode not present in traditional universal joints. If the universal joint were to axially align with the axis of the actuator, the actuator would completely lose command authority over the joint. The ball nut would freely spin as the trunnion rotated in its bearings. This issue forced the universal joint to be angled relative to the transversal plane.

The pitch axis of the joint could not be parallel to the transversal plane due to part interferences, but it needed to approach horizontal while still accommodating the range of motion. This led to a nominal angle of 86.5^o between the actuator and cross gimbal, which leaves a 19.2^o angle between the ball screw and cross gimbal when the universal joint is at the limit of its range of motion.

Lower Ankle Universal Joint

The lower ankle universal joint has the largest overall range of motion requirement on THOR. Since it is attached to the foot, the joint needs to be compact and lightweight. Table 2.5 shows the range of motion requirements for the ankle universal joints. Similar to the upper universal joints, the ankle joints are designed to be symmetric in roll to reduce the number of individual parts to be designed.

Table 2.5: Lower ankle universal joint range of motion requirements in degrees

Universal Joint Location	Min. Roll	Max. Roll	Min. Pitch	Max. Pitch
Ankle	–33.9	35.2	–38.5	54.1

Because it requires a larger range of motion, the pitch axis of the lower ankle universal joint is attached to the foot, while the roll axis is attached to the actuator. This arrangement simplified the design challenge to achieve the full range of motion, as it is possible to lengthen the trunnion to avoid interferences. An image of the lower ankle universal joint can be seen in Fig. 2.15.

This universal joint was designed to specifically meet the range of motion requirements of the lower ankle universal joint while avoiding part interferences with the shin at the extreme ends of the ankle motion. For example, the universal joint requires 54.1^o of max pitch motion. The lower ankle universal joint has a small factor of safety on angle range, as it is designed to allow for only 56^o of pitch before its two gimbals collide with one another. This design philosophy of small custom packaging also reduced the amount of material at the foot, decreasing the overall rotational inertia of the leg.

Figure 2.15: Lower universal joint for the ankle actuators.

2.2.4 Compliance

The elastic element is what delineates a rigid actuator from an SEA. Typical linear SEAs place a linear spring between either the motor and load or the motor and ground. Similar to its counterpart on SAFFiR, the THOR configurable compliant spring is an independent cantilevered titanium leaf spring [26]. Numerous actuators have used cantilevered springs as the compliant element [44], [45], [46], [47], [48]; however, the SAFFiR and THOR SEAs appear to be the first use of cantilever beams on a humanoid robot. The spring on SAFFiR is placed perpendicular to the main axis of the actuator, allowing the actuator to directly push on the beam. On THOR, the configurable compliant spring is located parallel to the main axis of the actuator. The two are connected through a rigid aluminum lever arm which also serves as a gimbal for th upper universal joint. An image of this connection can be seen in Fig. 2.16.

Not only does this parallel configuration of the spring relocate the space required for spring deflection away from the travel axis of the actuator, it takes advantage of load properties to reduce the size of the cantilever to achieve the same spring stiffness. The beam is moment loaded through the lever arm, allowing increased energy storage throughout the length of the beam compared to an identically sized cantilever loaded by a concentrated point load, such as with the SAFFiR SEA. This configuration is essential to supporting the larger actuator forces present on THOR.

Using the loading properties of a cantilever in pure bending, the spring dimensions were chosen as 6.5 x 38 mm with a configurable length. A removable pivot, shown in blue in Fig.

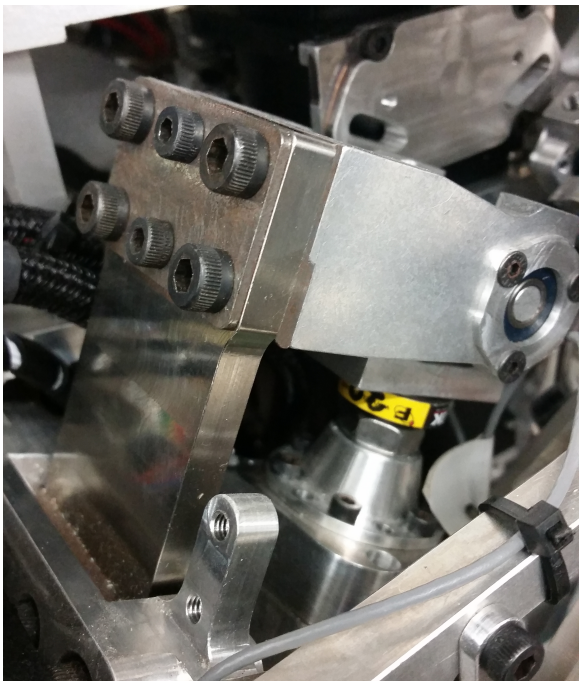

Figure 2.16: Actuator attachment to the configurable compliant spring.

2.17, allows for selection of a more stiff 650 kN/m or a more compliant 372 kN/m spring stiffness rate by adjusting the effective length of the cantilever. In addition, a lockout can be mounted between each spring lever arm and the robot frame, preventing spring deflection.

Each compliant spring uses the same interface to attach to the structure of THOR. This universal interface expedited the design process and simplified the manufacture. In addition to the identical structural interfaces, each lever arm connecting the compliant beam to the actuator is the same.

As shown in the exploded view of the compliant beam in Fig. 2.18, a set of custom steel washers interface between the aluminum and titanium to ensure a rigid attachment between the lever arm and beam. A boss on the base of the lever seats within the boss of the top washer, which in turn seats within the slot on the titanium beam. This arrangement loads the bolts axially rather than in shear, and the stepped bosses aim to reduce stress concentrations within the aluminum lever.

Spring Stiffness and Deflection Path

Analytically determining the spring stiffness requires a cantilever beam model solved using superposition. Fig. 2.19 shows the titanium beam free body diagram (FBD) for the complex loading case. Table 2.6 lists the dimensions of the compliant beam.

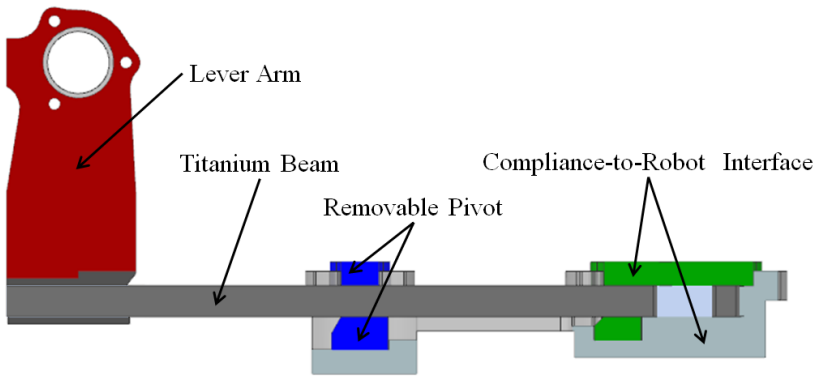

Figure 2.17: Cutaway view of the configurable compliant member. The blue pivots are removable to change the stiffness of the spring.

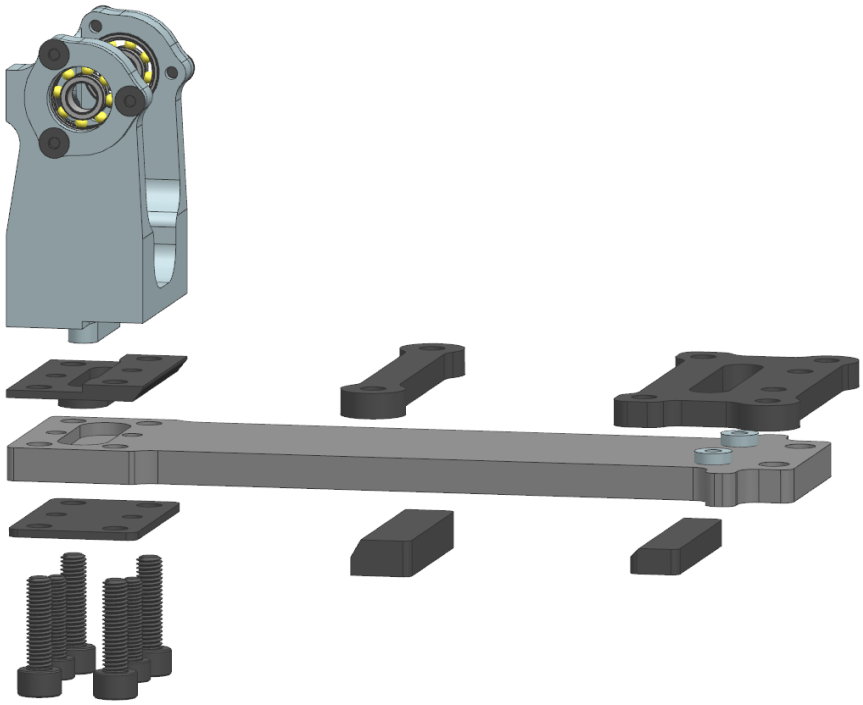

Figure 2.18: Exploded view of the compliant beam assembly.

Table 2.6: Dimensions of the compliant beam, as labeled in Fig. 2.19.

Dimension	Length (mm)
t	6.5
l	110.2 or 55.15
d	38
h	50

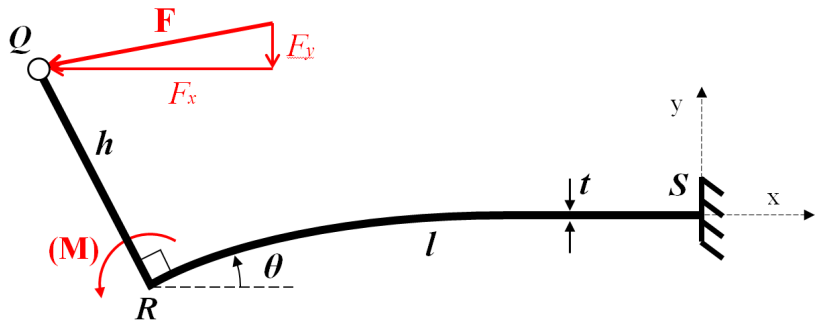

Figure 2.19: Free body diagram of the compliant beam in loading.

The effective stiffness of the spring can be calculated using the deflection path:

$$k_{eff} = \frac{|F|}{\sqrt{\Delta Q_x^2 + \Delta Q_y^2}} \tag{2.1}$$

The axial load creates deflections only in the x-direction:

$$\Delta x_a = \frac{-F_x l}{EA} \tag{2.2}$$

Deflection resulting from bending loads is:

$$\Delta y_b = \frac{-F_y l^3}{3EI} \tag{2.3}$$

$$\frac{dy}{dx}_b = \frac{F_y l^2}{2EI} \tag{2.4}$$

Deflection resulting from the moment load, M, is:

$$\Delta y_m = \frac{-F_x h l^2}{2EI} \tag{2.5}$$

$$\frac{dy}{dx}_m = \frac{F_x h l}{EI} \tag{2.6}$$

Based on the geometry of the compliant member, the deflection of point Q from nominal is:

$$\Delta Q_x = \Delta x_R - h \sin\theta_R = \Delta x_a - h \sin\left(\frac{dy}{dx}_b + \frac{dy}{dx}_m\right) \tag{2.7}$$

$$\Delta Q_y = \Delta y_R - h\left(1 - \cos\theta\right) = \Delta y_b + \Delta y_m - h\left(1 - \cos\left(\frac{dy}{dx}_b + \frac{dy}{dx}_m\right)\right) \tag{2.8}$$

Fig. 2.20 shows the deflection path of point Q for both stiffness settings of the cantilever. Fig. 2.21 shows the cantilever deflection across the commandable range of forces for both compliance settings; the slope of each line is the effective stiffness caclulated using 2.1. The stiffness analysis of the beam is highly sensitive to the effective length chosen for the beam, which is difficult to model given the complex attachment of the lever arm. Using the dimensions from Table 2.6 the average effective analytical stiffnesses of the beam are approximately 635 kN/m for the stiff setting and 245 kN/m for the compliant setting. Actual data from spring deflection experiments yield actual stiffnesses of 655 and 372 kN/m, respectively. The difference in the analytical and experimental results likely lies within the mechanical properties of the titanium as well as the effective lengths chosen for the analytical solution.

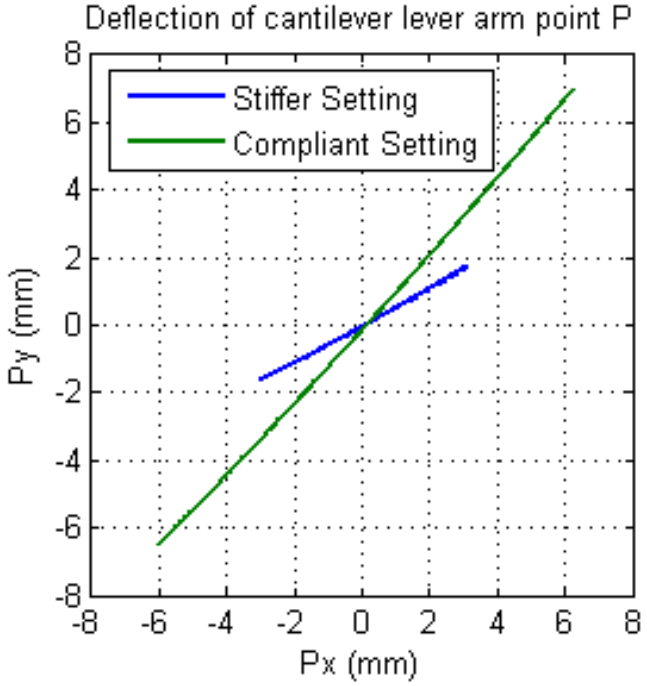

Figure 2.20: Analytical cantilever deflection path calculated for both compliance settings.

2.3 Electrical Design

This section overviews the design of a custom dual-axis motor controller used to implement compliant joint-space control for the hip and ankle joints. The "motor slug" shown in Fig. 2.22 implements sensor processing, current control, actuator impedance control, and joint-space impedance control on a single microprocessor. This custom controller sends pulse width modulated (PWM) signals to a pair of servo drives which control electrical current in the Maxon BLDC motor driving each actuator on the robot.

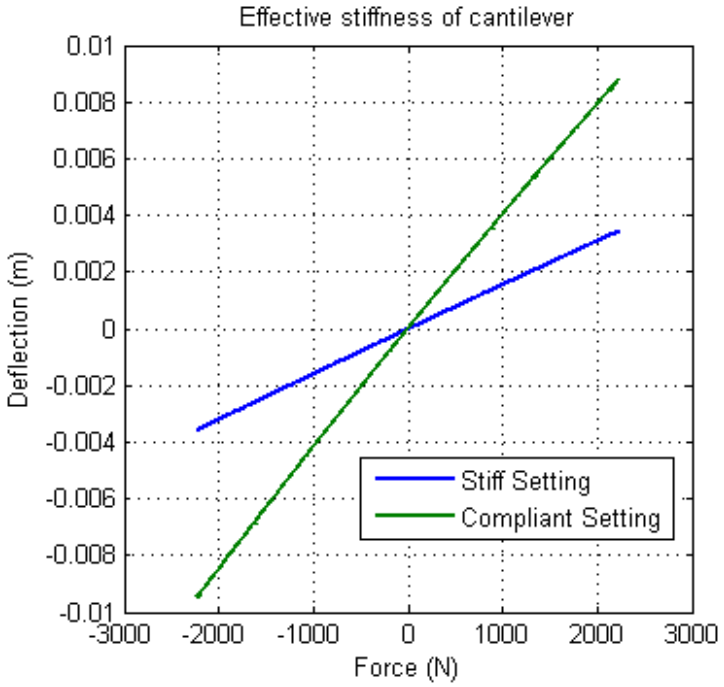

Figure 2.21: Analytical cantilever deflection plotted over input force.

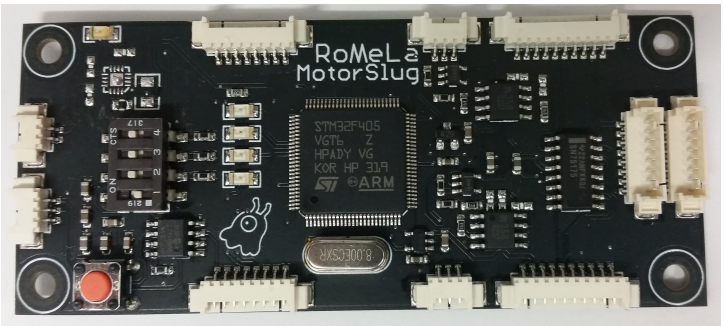

Figure 2.22: Custom dual-axis motor controller for compliant control of parallel actuated joints.

As seen in Fig. 2.22 the hardware design is centered around a 32-bit ARM Cortex-M4 processor. The microcontroller interfaces to absolute encoders mounted to each joint axis and incremental encoders attached to each actuator motor, as well as the in-line actuator load cell sensors. The motor controller runs the dual-axis joint torque control loop at 400 Hz. Further details of the dual axis motor controller design can be found in [49].

2.3.1 Sensor Selection

Table 2.7 details the sensor specifications of the SEA sensors in terms of actuator measurements, such as actuator force and length resolution. Sensor performance is suitable for high-bandwidth joint impedance control.

Table 2.7: Performance specifications of sensors used on the THOR SEA

	Futek LCM200	Gurley A19	Maxon #225780
Sensor Type	Load Cell	Absolute Encoder	Incremental Encoder
Measurement	Actuator Force	Joint Angle	Actuator Length
Range	+/- 2225 N	0 - 2 π	Continuous
Resolution	+/- 2 N	0.66 arcmin	4.19 μm
Maximum Speed	-	2400 RPM	0.84 m/s
I/O Protocol	Analog Voltage	Gray Code	TTL

2.4 Actuator Analysis

Fig. 2.23 shows actuator performance specifications derived from the Maxon motor data sheet and scaled through the actuator gearing ratio. The maximum continuous force is 685 N, the peak force is limited by the load cell and universal joint bearings to 2225 N, and the no-load speed is 0.198 m/s.

2.4.1 Hip Roll/Yaw Joint

The range of motion in the parallel hip joint is listed in Table 2.8. The peak roll and yaw torques available through this ROM are shown in Figures 2.24 and 2.25, respectively. Maximum torques are calculated by summing the individual peak torques applied at the two lever arms in the parallel joint assembly. Joint statics over the range of motion in the hip are solved using a kinematic model to determine the cross products between the actuators and lever arms, scaled to the peak actuator force.

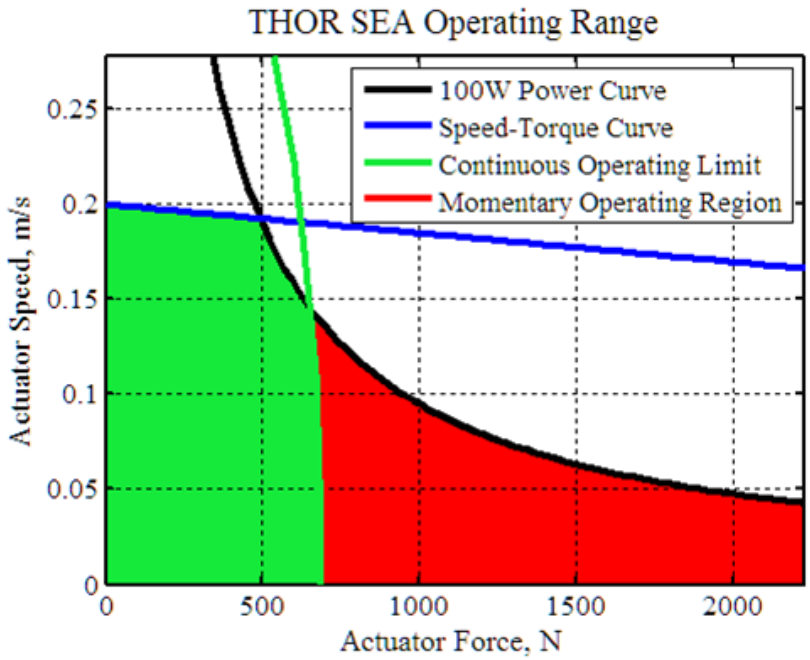

Figure 2.23: Actuator power-speed-torque curves generated from Maxon BLDC data sheet. The continuous operating region is shaded in red.

Table 2.8: Range of motion of the THOR hip roll/yaw joint

	Minimum Angle (deg)	Maximum Angle (deg)	Peak Torque (Nm)
Hip Roll	–30	45	194
Hip Yaw	–20	45	128

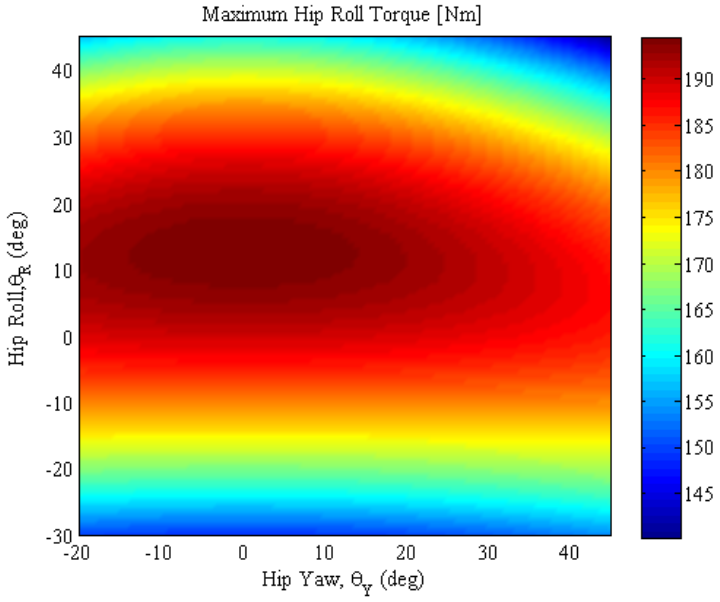

Figure 2.24: Peak roll torque over the hip range of motion.

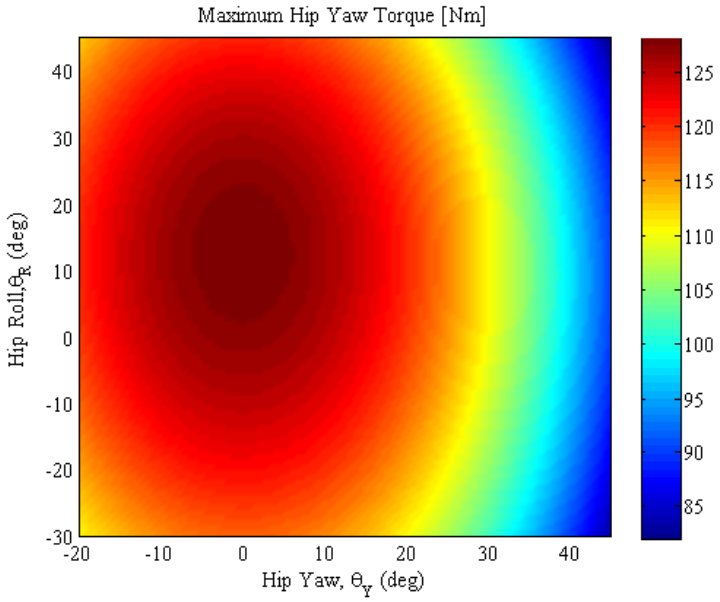

Figure 2.25: Peak yaw torque over the hip range of motion.

2.4.2 Ankle Pitch/Roll Joint

The range of motion in the parallel ankle joint is listed in Table 2.9. The peak pitch and roll torques available through this ROM are shown in Figures 2.26 and 2.27, respectively. The maximum torque profile is calculated in the same method described in Section 2.4.1

Table 2.9: Range of motion of the THOR ankle pitch/roll joint

	Minimum Angle (deg)	Maximum Angle (deg)	Peak Torque (Nm)
Ankle Pitch	–55	35	323
Ankle Roll	–30	30	246

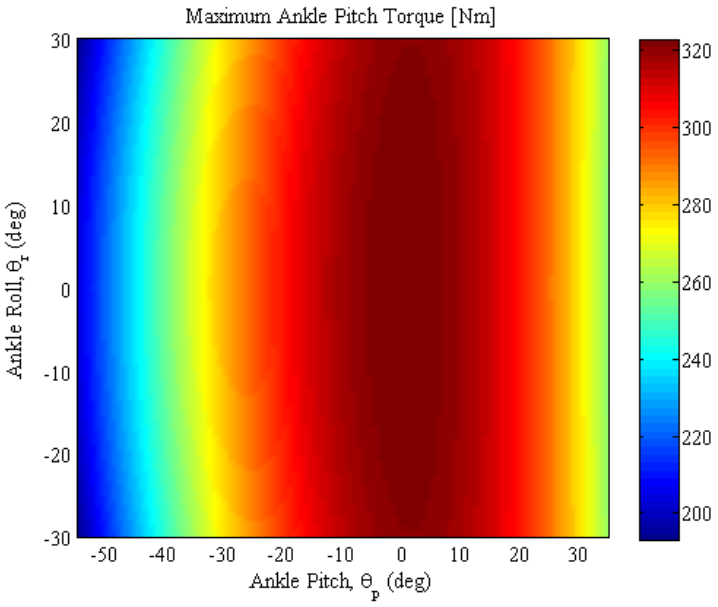

Figure 2.26: Peak pitch torque over the ankle range of motion.

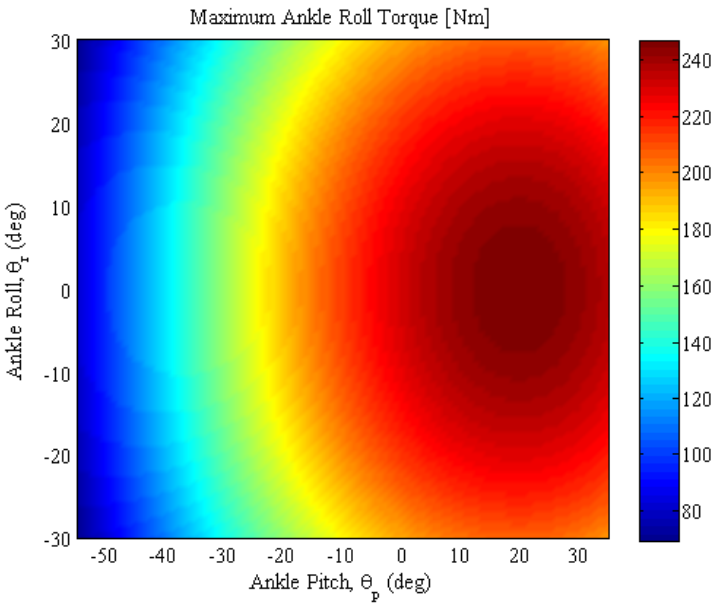

Figure 2.27: Peak roll torque over the ankle range of motion.

Chapter 3

Straight Line Mechanism

3.1 Introduction

Rescue tasks require not only a human-like range of motion in the lower body, but also a large amount of torque throughout those ranges. The THOR design aims to have sufficient range of motion and torque required for rescue robotics. The hip and ankle joints of THOR connect the actuator output to a crank arm, which delivers peak torque near the nominal configuration [9]. Toward the limits of the range of motion, however, there is a significant decline in torque output as the mechanical advantage of the lever arm deteriorates. Since the knee and hip pitch joints require rotation exceeding 135^o, as opposed to other joints which move up to 90^o, achieving both range of motion and torque necessitated an innovative actuation strategy.

While rotary SEAs can offer a constant torque profile and continuous rotation, designing two vastly different actuators was not appropriate considering the accelerated pace at which THOR was developed. Many robotic joints driven by linear actuators utilize a cable transmission to remotely power a rotary joint [37], [38], [39], [40], but face issues of cable stretch, creep, tensioning, wear, and temperature sensitivity. Instead, a linear-to-rotary conversion mechanism was paired with the already designed linear SEA on THOR to increase the usable range of motion at the hip pitch and knee joints. Several mechanisms were evaluated, including rack and pinions, slider cranks, cabling, and planar straight-line mechanisms such as the Watt, Chebyshev, Evans, Peauceillier-Lipkin, and Hoeken's linkages. Each of these linear-to-rotary converters has its detriments, but an inverted Hoeken's four-bar linkage was best suited for this application due to its large crank angle range for a relatively short linear input.

The Hoeken's linkage, depicted in Fig. 3.1, is a well-documented four-bar crank rocker mechanism typically used to approximate linear motion from a rotary input. The kinematics of the Hoeken's mechanism have been studied extensively [50] [51] [52], noting the trade-off in

linearity for constant velocity. In [50], Norton provides a table of link length ratios optimized for either constant velocity or linearity. Bulatović optimizes both speed and linearity of the linkage through the addition of an eccentrically geared crank input [52].

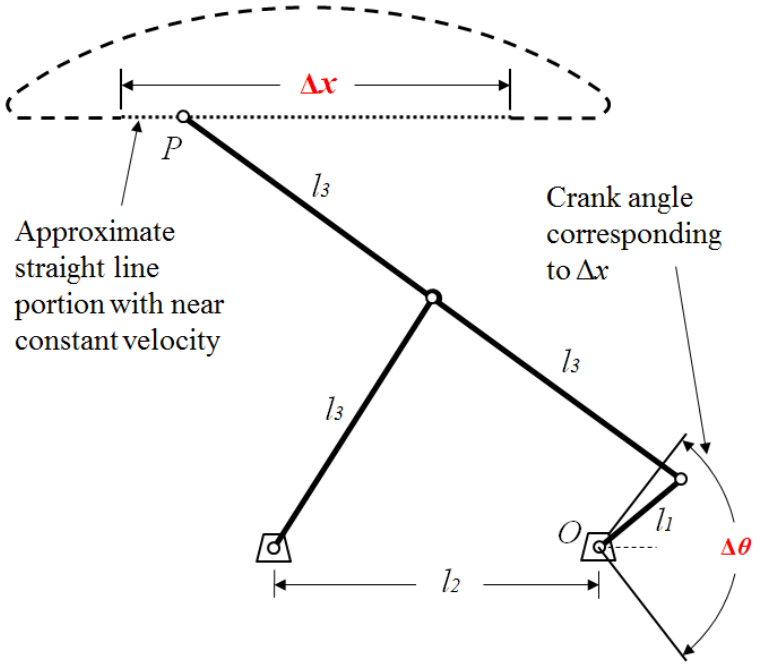

Figure 3.1: Hoeken's linkage schematic.

The Hoeken's linkage has been used in many robotic applications. Breen combines the linkage with a rotary motor to create an active vibration controller for automobile seats [53]. Barlas pairs two Hoeken's mechanisms to create a rocker-bogie transmission for a Mars rover suspension [54]. The end effector presented by Rodriguez features the linkage to realize 1-DOF planar actuation [55]. A number of other applications have used the Hoeken's linkage in a similar fashion [56] [57] [58] [59] [60]. The mechanism utilized on THOR follows optimized link length ratios detailed in Norton; however, it utilizes the Hoeken's linkage in an inverted configuration dissimilar to all previous applications.

This chapter overviews the synthesis, design, and joint torque analysis of the inverted Hoeken's linkage used in the knee and hip pitch joints on THOR to address the range of motion and mechanical advantage limitations of linear SEAs. The first section overviews the mechanism synthesis and derives the kinematic equations of motion. The second section overviews the design of the inverted Hoeken's mechanism and its incorporation into the thigh structure. The final section explores the implications of inverting the mechanism, specifically, the deviation in the nominal torque profile resulting from cantilever deflection of the input SEA.

3.2 Synthesis

While the general solution of the Hoeken's linkage is ubiquitous, it was necessary to determine the motion of and forces within each link for design and packaging purposes. The kinematics of the Hoeken's linkage are solved below using a geometric analysis based on Fig. 3.2.

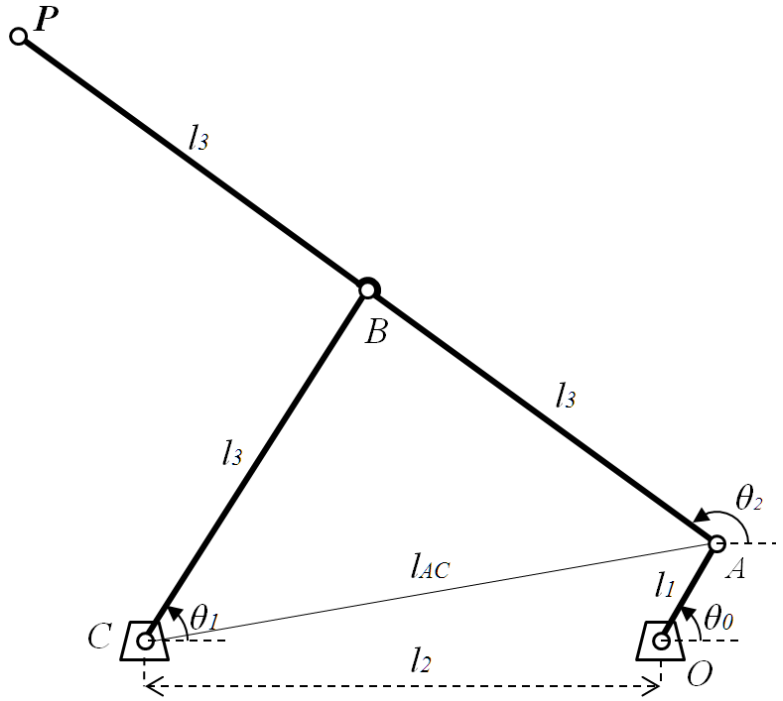

Figure 3.2: Hoeken's linkage schematic used for geometric analysis.

3.2.1 Position Analysis

$$l_{AC} = \sqrt{l_1^2 + l_2^2 + 2l_1 l_2 \cos\theta_O} \tag{3.1}$$

$$\angle ACO = \arctan\left(\frac{l_1 \sin\theta_O}{l_1 \cos\theta_O + l_2}\right) \tag{3.2}$$

Using the law of cosines,

$$\angle ABC = \arccos\left(1 - \frac{{l_{AC}}^2}{2{l_3}^2}\right) \tag{3.3}$$

$$\angle BCA = \arccos\left(\frac{l_{AC}}{2l_3}\right) \tag{3.4}$$

$$\theta_1 = \angle BCA + \angle ACO \tag{3.5}$$

$$\theta_2 = \angle ABC + \theta_1 \tag{3.6}$$

With the link angles solved, the travel of point P is described by

$$P_x = l_1 \cos\theta_O + 2l_3 \cos\theta_2 \tag{3.7}$$

$$P_y = l_1 \sin\theta_O + 2l_3 \sin\theta_2 \tag{3.8}$$

These equations hold true for $-\pi/2 < \theta_O < \pi/2$, which covers the entire usable region of the linkage.

3.2.2 Force Analysis

The force analysis is solved below using the free-body diagram (FBD) of the linkage, shown in Fig. 3.3.

Summing horizontal and vertical forces in link AP reveals:

$$R_{Ax} = -F_x - R_{Bx} = -F\cos\theta_F - R_{Bx} \tag{3.9}$$

$$R_{Ay} = -F_x - R_{By} = -F\sin\theta_F - R_{By} \tag{3.10}$$

Summing moments in link AP about point A gives:

$$(2F_x + R_{Bx})\sin\alpha + (2F_y + R_{By})\cos\alpha = 0 \tag{3.11}$$

Since link BC is a two-force member:

$$R_{By} = R_{Bx}\tan\theta_1 \tag{3.12}$$

Combining equations 3.93.103.113.12 gives solutions for the reaction forces at joint A,

$$R_{Ax} = -F\cos\theta_F + 2F\frac{\sin\alpha\cos\theta_F + \cos\alpha\sin\theta_F}{\sin\alpha + \cos\alpha\tan\theta_1} \tag{3.13}$$

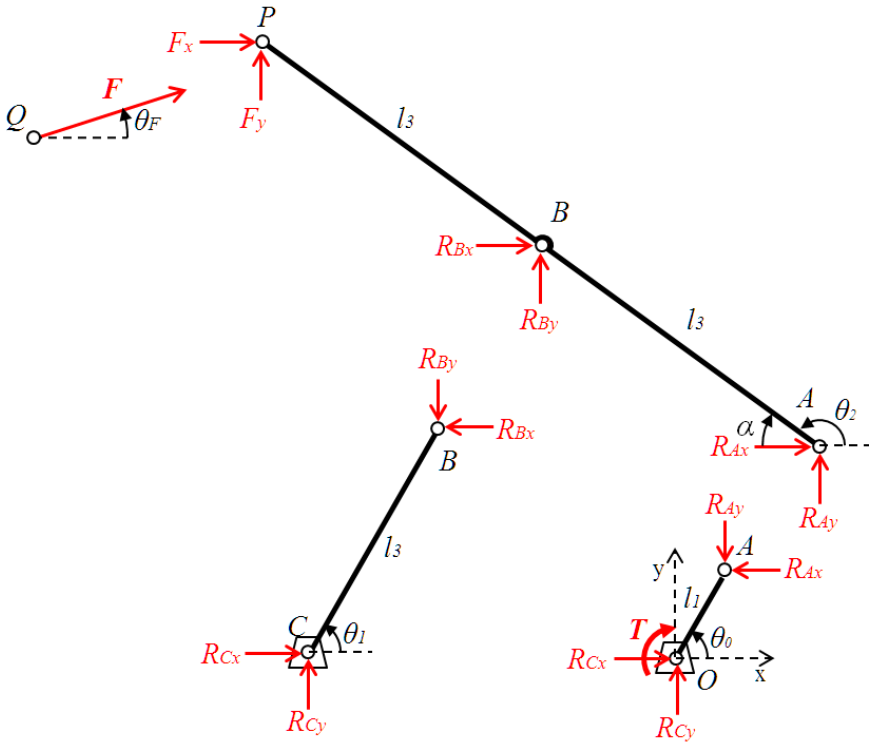

Figure 3.3: Free body diagram of Hoeken's linkage.

$$R_{Ay} = -F \sin\theta_F + 2F \frac{\sin\alpha\cos\theta_F + \cos\alpha\sin\theta_F}{\sin\alpha + \cos\alpha\tan\theta_1} \tan\theta_1 \tag{3.14}$$

where is the angle at which force is applied to point P. Summing moments in link AO about point O gives:

$$T = l_1 \left(R_{Ax}\sin\theta_0 - R_{Ay}\cos\theta_0\right) \tag{3.15}$$

Substitution of 3.13 and 3.14 into 3.15 results in a solution for output torque as a function of known joint angles and an input force along θ_F. This solution holds true for crank angles between –90^o and +90^o.

A MATLAB script was written to solve and simulate the position of the linkage through its designed range of motion, and to compute the maximum forces in each link and bearing given a unit force input. Fig. 3.4 shows the results output from one such simulation. For initial design verification the angle of the force input, θ_F, was fixed at 0^o.

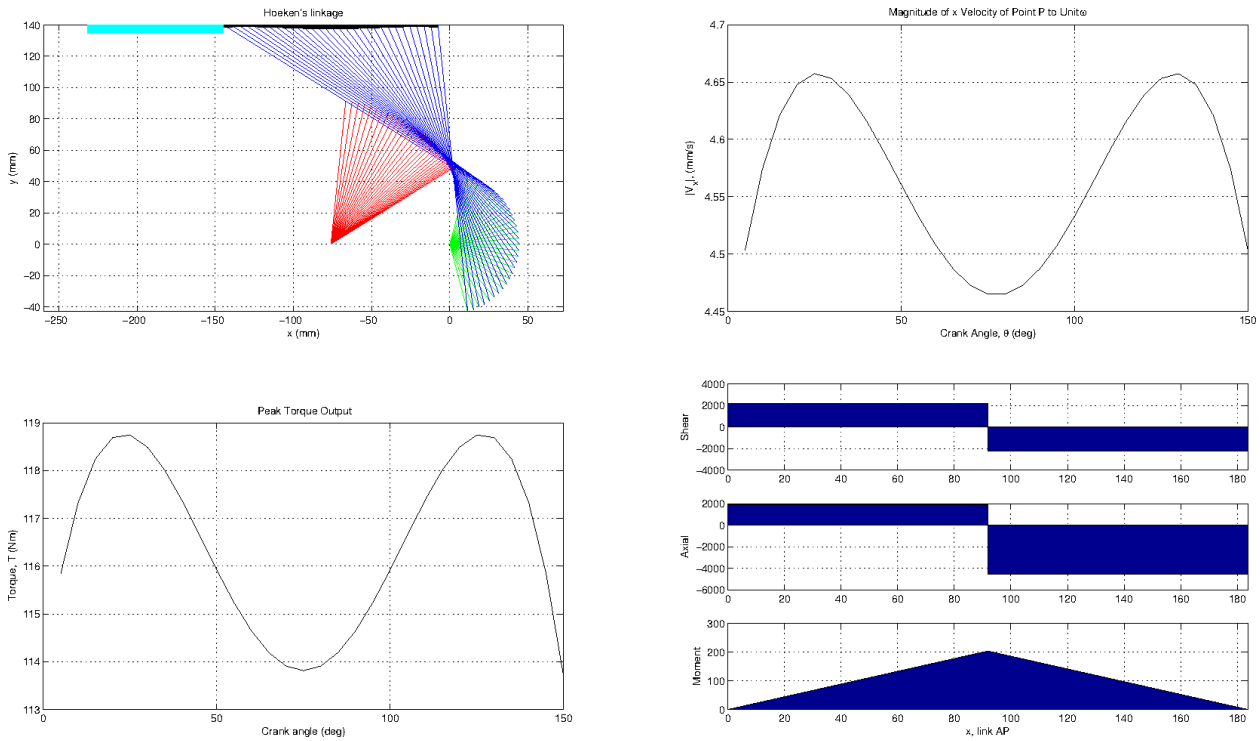

Figure 3.4: Data output window from MATLAB Hoeken's design simulator.

3.3 Design

For THOR link length ratios were chosen from [50] which optimize the velocity, and therefore the output torque, of the linkage throughout a crank angle range of 150^o. As with all crank-

arm linkages the torque output is directly proportional to the length of the crank lever arm, so the crank arm was sized until the peak output torque corresponding to the SEA's 2225 N peak force reached the goal specification of 115 Nm. The resulting link lengths are given in Table 3.1.

Table 3.1: Link lengths of Hoeken's mechanism

l1 (mm)	l2 (mm)	l3 (mm)	Δ x (mm)
44.4	76	91.9	136.8

Fig. 3.5 shows the trajectory of point P on the Hoeken's linkage throughout its range of motion on THOR. The optimized link lengths result in a deviation of less than 1% from a linear trajectory, and an output angular velocity deviation of 4.25% from constant. The point trajectory is used to determine the pitch angle range of the upper universal joints as well as the required travel length of the ball screw, Δx.

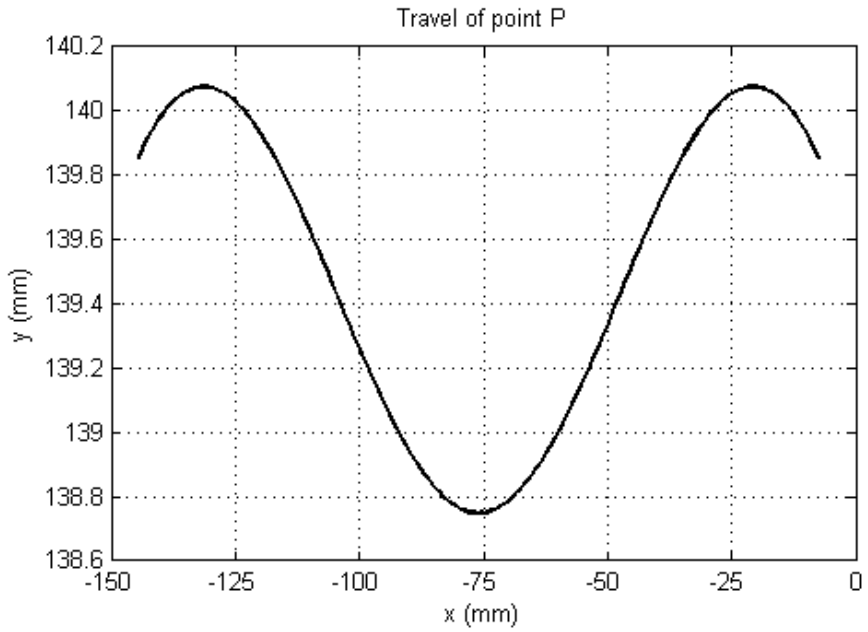

Figure 3.5: Trajectory of point P through the range of motion on THOR.

3.3.1 Bearing Selection

Following the static force analysis of the Hoeken's linkage described in Section 3.2.2, the force distribution within each link was calculated to determine bearing and link load requirements. Each joint in the linkage was loaded in double-shear to reduce individual bearing loads, prevent harmful torsion loads in the links, and assist in preloading the bearings to eliminate

backlash. Table 3.2 lists the radial bearings used in each joint within the linkage, including the maximum forces applied to each joint from a 2225 N input force, and the static and dynamic load ratings of each bearing. Note that the maximum applied load to each bearing accounts for each joint loaded in double support.

Table 3.2: Bearings used within the Hoeken's Linkage on THOR

Joint	Bearing	Dimensions (mm)	Max. Applied Force (N)	Static Load Rating (N)	Dynamic Load Rating (N)
O	MR6000–2RS	10x26x8	1625	1962	4551
A	MR6800–2RS	10x19x5	1625	834	1717
B	MR608–2RS	8x22x7	2461	1383	3296
C	MR6900–2RS	10x22x6	2461	1275	2698
P	MR696–2RS	6x15x5	1113	520	1344

Nearly every bearing in the linkage is loaded beyond its static load rating yet below its dynamic rating. The decision to overload the bearings was made to reduce sizing and weight of the links through the use of smaller bearings. While the bearings will endure minute plastic deformation while at peak load, maintaining peak loads within the dynamic rating will give the bearings a life cycle longer than the proposed lifetime of the robot.

3.3.2 Linkage Packaging

The linear SEAs described in Section 2.2 were modified to replace the load bearing carbon fiber tube with a trunnion attached directly to the ball nut to act as the interface to the Hoeken's linkage. A rendering of the hip pitch actuator is shown in Fig. 3.6. The length of the ball screw was determined based on the travel length of the Hoeken's linkage, Δ_x, which was only 3 mm shorter than the requirement for THOR ankle ball screws. This coincidence enabled the use of same ball screws for both the thigh actuators and ankle actuators, saving on manufacturing costs.

The actuators are mounted in the thigh at the same angle, to ease manufacture of the compliance-to-robot interface. Many of the links are designed with a non-linear shape in order to avoid interferences throughout the range of motion. Figs. 3.7 and 3.8 show the side and front views, respectively, of the Hoeken's linkage in the knee and hip pitch joints.

The width of the hip joint is greatly dependent on the width of the hip pitch linkage, so design efforts focused on reducing the width of the hip linkage to less than the width of

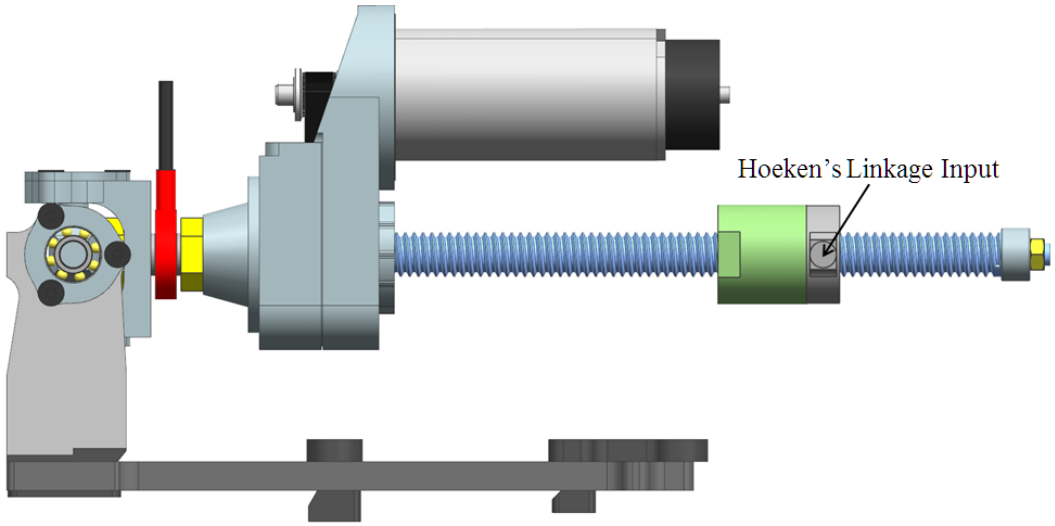

Figure 3.6: Hip pitch actuator, highlighting the ball nut trunnion interface to the Hoeken's linkage.

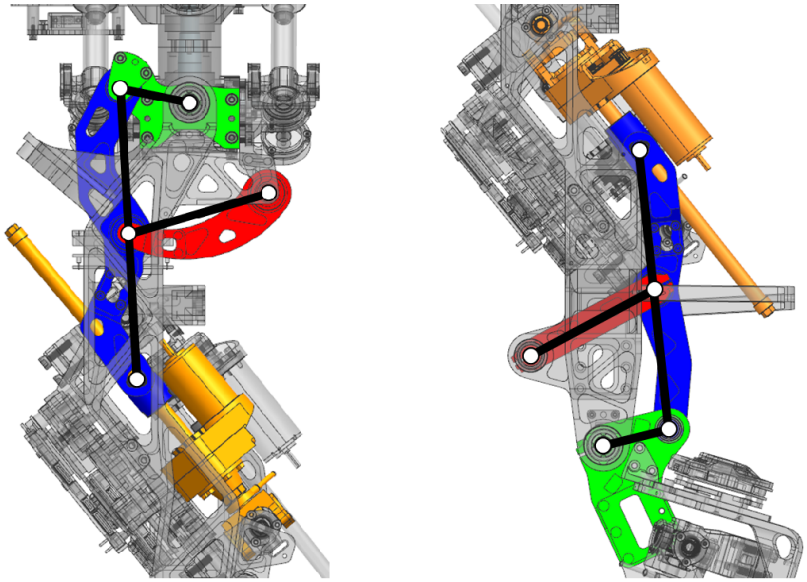

Figure 3.7: Side views of Hoeken's mechanism in its nominal configuration packaged within thigh for the hip pitch (left) and knee pitch (right) joints, overlain with a schematic of the Hoeken's linkage.

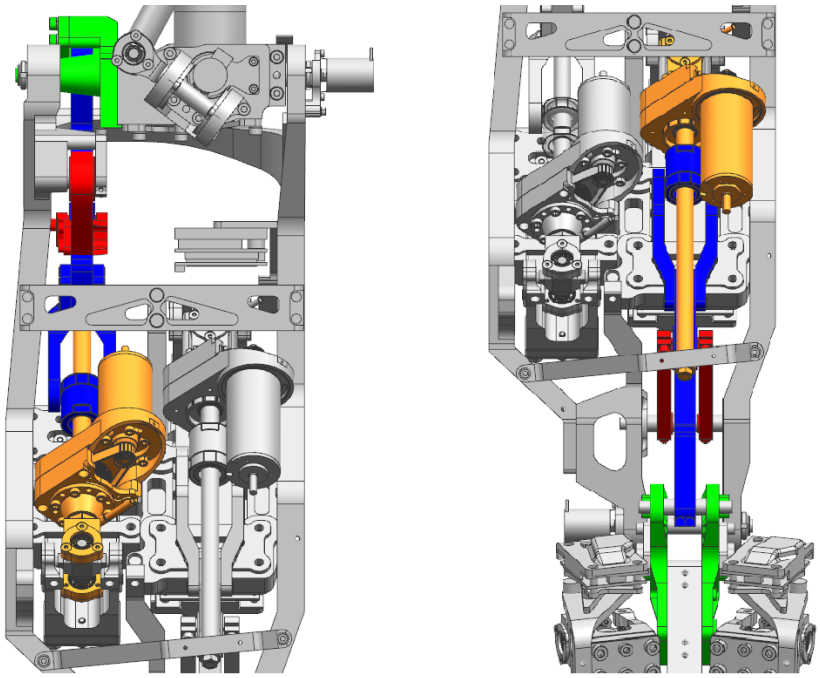

Figure 3.8: Front views of Hoeken's mechanism for the hip pitch (left) and knee pitch (right) joints.

the SEA: 0.041 m. Making the hip linkage thin results in increased difficulty of repairs, as essentially the entire leg must be dismantled to replace any part. The width of the knee linkage is wider, 0.065 m, allowing for easier repairs through removal of the bearing shafts. Though the final rotary packages are quite thin, they occupy a large area footprint. For this reason, they cannot be used in other joints.

Figs. 3.9 and 3.10 display the motion of the linkage through the hip pitch and knee ranges of motion, respectively. The hip pitch linkage produces joint motion from -120^o to $+30^o$. Though the knee linkage is designed for 150^o of crank rotation, structural interferences between the calf and thigh reduced the knee joint rotation to 135^o.

The addition of the inverted Hoeken's linkage to the SEA successfully augments the output joint range of motion to 150^o. Since the actuator is supported through a universal joint on one side, the actuator can pitch and roll to accommodate linearity errors and compensates for any variance in the machining or assembly process.

3.4 Mechanical Advantage

The angular velocity and linearity errors intrinsic to the Hoeken's linkage create a small deviation in the mechanical advantage of the mechanism along its range of motion. Furthermore,

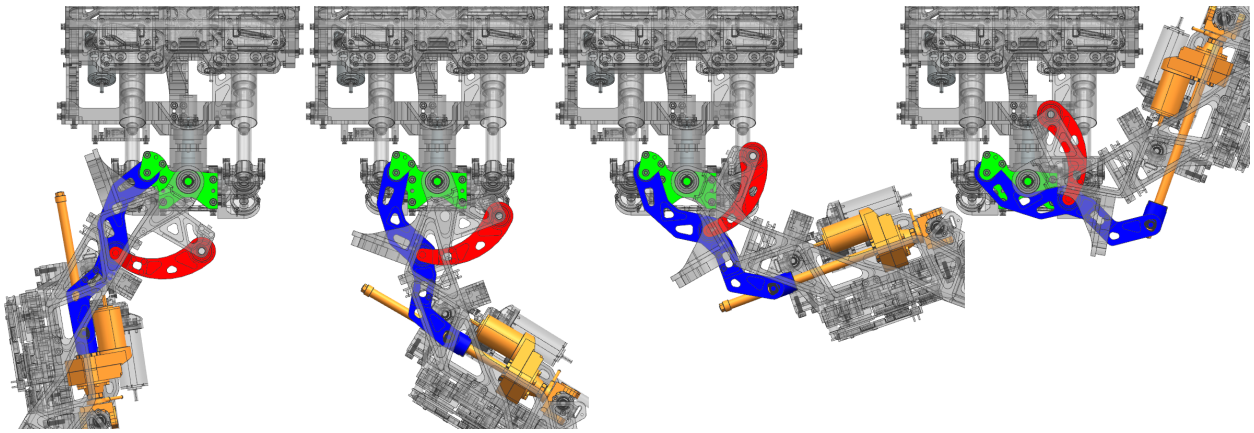

Figure 3.9: Hip pitch Hoeken's linkage at –120^o, –60^o, 0^o, and 30^o.

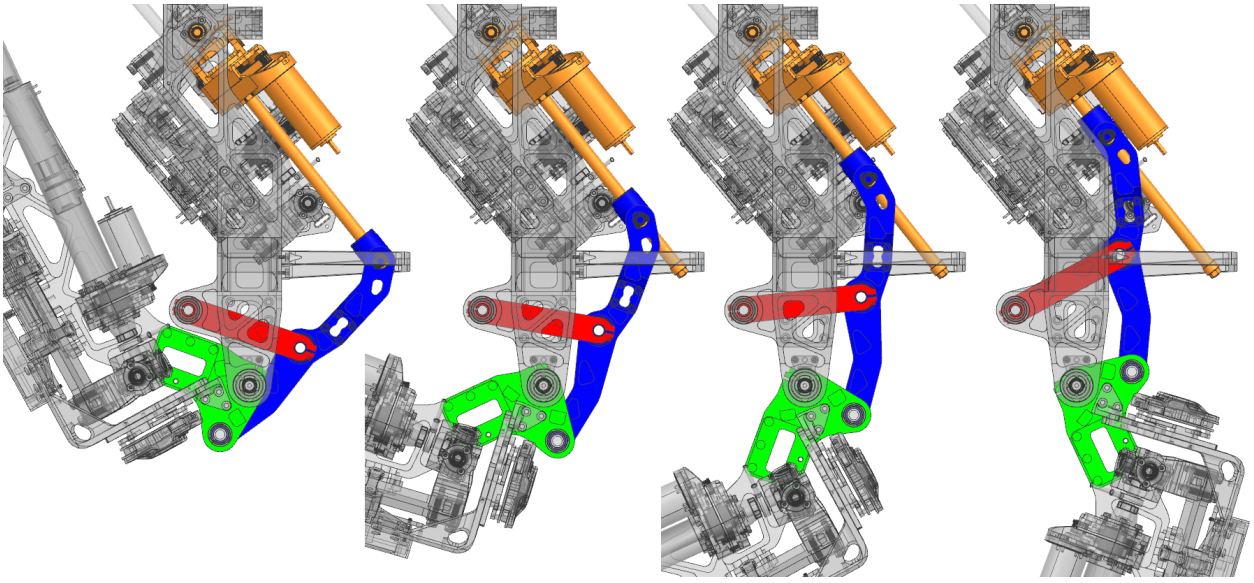

Figure 3.10: Knee Hoeken's linkage at 135^o, 90^o, 45^o, and 0^o.

cantilever deflection under load introduces deviation from the nominal torque output curve. A mechanical advantage lookup table is used to compute nominal feedforward joint torques from measured joint angle. Coupling data from the in-line load cell and an absolute optical encoder at the output joint enable robust force control of the knee and hip pitch joints.

Despite actuator linear displacement being the input to the Hoeken's linkage, proprioceptive data obtained from the absolute joint encoder and load cell greatly simplify calculations for the torque profile. Therefore, all derivations are functions of these sensor readings. Fig. 3.11 shows the knee rotary actuator package overlaid with the schematic used for calculations in this section. Calculations are based on a generic crank angle, which are phase shifted for use on the knee and hip pitch joints depending on their nominal configuration on THOR.

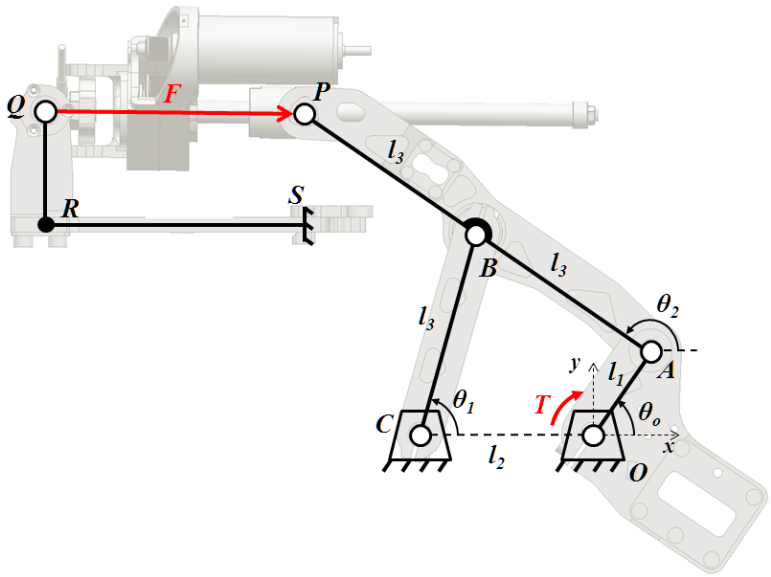

Figure 3.11: Schematic of SEA and Hoeken's linkage overlaid on knee joint.

3.4.1 Nominal Performance

To generate the lookup table for computing feedforward joint torques, the Hoeken's linkage was decoupled from the actuator and a unit force vector along $\overrightarrow{QP}$ was used as the input, as described in Section 3.2.2. The nominal coordinates of the actuator upper universal joint, point Q, relative to the hip pitch and knee joints are listed in Table 3.3. Fig. 3.12 shows the nominal mechanical advantage profile across a crank angle range of 150^o using link lengths from Table 3.1 for the hip pitch joint; the profile for the knee joint is nearly identical.

Since the feedforward torque is computed using the nominal mechanical advantage lookup table, torque errors arise from deflection of the cantilever beam under load. A 2-dimensional lookup table based on both force input and joint angle could compensate for these errors, at

Table 3.3: Relative locations of actuator upper universal joints on hip pitch and knee joints

Joint	Q_x (m)	Q_y (m)
Hip Pitch	–0.2321	0.1413
Knee	–0.2391	0.1415

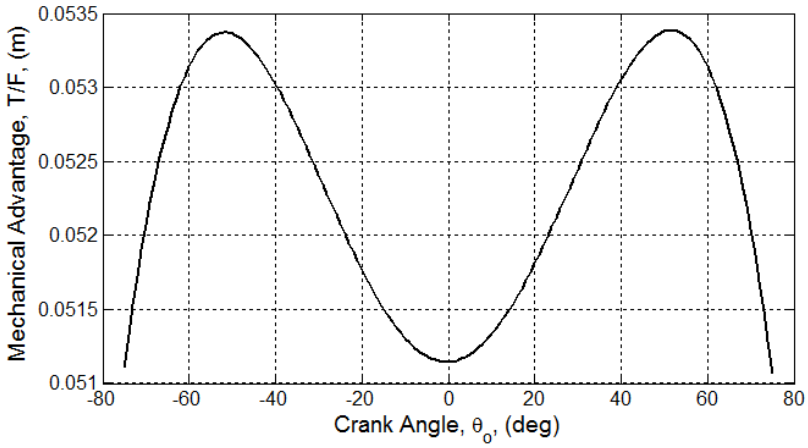

Figure 3.12: Nominal mechanical advantage profile of THOR Hoeken's linkage in the hip pitch joint.

the trade-off of computational performance. While the 1-dimensional lookup table can easily be handled by the custom motor controllers, it is imperative to know worst-case deviation from nominal mechanical advantage prior to committing to the use of a 2-dimensional lookup table.

3.4.2 Under Load

The percentage deviation from the nominal mechanical advantage profile was computed using the derivations from Section 3.2.2 after determining worst-case deflection of point Q from a simplified cantilever beam model. The mechanical advantage profiles were recalculated, incorporating the resulting cantilever deflections. Fig. 3.13 shows the percent error that these two cases deviate from the nominal mechanical advantage profile.

The mechanical advantage error stays within 0.25% for the majority of the range of motion, and only exceeds this at the end of the motion. The maximum deviation from the nominal profile is –0.62%, which occurs at maximum joint deflection. Therefore, feedforward torque compensation can be accomplished using a single mechanical advantage lookup table without any significant loss in performance.

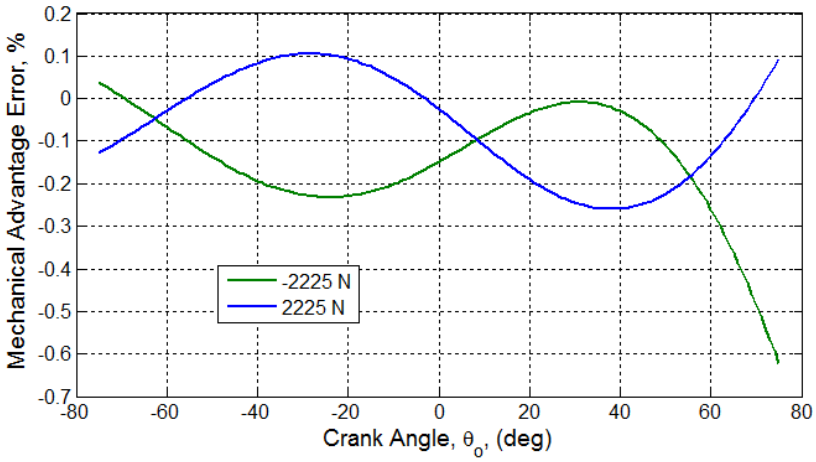

Figure 3.13: Percentage deviation from nominal mechanical advantage profile due to worst-case cantilever deflection.

3.4.3 Torque Profile

The peak and continuous torque curves for the Hoeken's actuators are plotted in Fig. 3.14. The average peak torque output is 116 Nm, while the average continuous torque output is 36 Nm. The knee pitch actuator uses a 200W motor to slightly increase the continuous torque available on the robot to approximately 39 Nm.

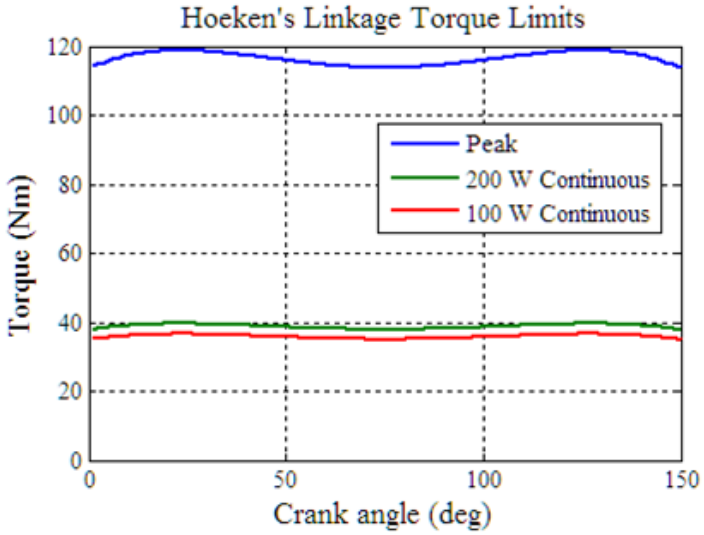

Figure 3.14: Torque profile of the Hoeken's linkage used in the hip pitch joint on THOR.

Chapter 4

Conclusion

Three different configurations of a ball screw driven linear series elastic actuator were designed for use on a full-sized humanoid disaster response robot, THOR. The 100 W actuator delivers a 2225 N peak load and can travel up to 0.198 m/s. The hip roll/yaw and ankle pitch/roll joints are driven by two linear SEAs each, arranged in a parallel configuration. These joints each feature a large workspace and sufficient torque to support bipedal locomotion. The SEAs are a critical subsystem that enables THOR to utilize an advanced whole-body controller to reliably traverse uneven terrain.

The hip pitch and knee pitch joints are serially driven by a linear SEA paired with a novel inverted Hoeken's straight-line linkage to convert actuator translation into joint rotation. The addition of this mechanism augments the available joint torque and range of motion. The linkage provides a nearly constant mechanical advantage and peak torque of 116 Nm throughout the 150^o range of motion.

4.1 Recommendations

Most of the design considerations for the THOR SEA were selected to minimize size and weight of the actuator. Given a more relaxed design space for a new linear SEA, a few key modifications would improve the actuator design and performance. First, designing a single universal SEA design for use across an entire platform would drastically reduce the cost and work load of development and assembly.

Second, the bearings used in the bearing housing do not entirely constrain radial tipping of the ball screw because of the inability to preload the radial bearings. At a sacrifice to the actuator zero-stroke length, using sufficiently large angular contact bearings or cross-roller bearings would further reduce backlash and radial play of the ball screw.

Furthermore, the manufacture of the PTFE bushing used to prevent ball nut tipping is a

tedious process. The PTFE is difficult to machine to proper tolerance, given the compliant nature of the material. A future design could investigate other low friction bushing materials and designs that are easier to manufacture. Alternatively, the ball nut can be constrained using linear guides similar to other linear SEA designs, at the detriment of added friction, weight, and packaging space.

4.2 Mechanical Failure Modes

A few notable failure modes have been identified on the THOR SEA through rigorous testing on the robot. Many of these failure modes can be avoided through careful redesign and assembly. If there is not sufficient belt tension between the speed reduction pulleys, the timing belt teeth can slip and eventually wear at high torques. While the eccentric motor mount provides an effective means of setting and maintaining belt tension, monitoring belt tension and wear should be included in the actuator maintenance process.

One of the most catastrophic failure modes is when the actuator is driven beyond its designed travel limits. Driving the ball nut into the base of the bearing housing can cause damage to the ball screw threads and can introduce backlash into the precision ball nut interface, while driving the ball nut off the free end of the ball screw can lead to separation and irreparable damage to the ball screw assembly. To prevent this from occurring, mechanical hard stops were implemented on THOR to limit the joint ranges of motion to within the travel limits of each actuator.

The final major mode of failure is unexpected impacts and side loads on the actuator. On one occasion, the right foot of THOR kicked the back of the calf, impacting the carbon fiber load transmission tube of an ankle actuator and bending the Futek load cell. While the universal joints effectively eliminate bending loads through the actuator, they are not design for side impacts. Incorporating covers around exposed actuator components on the robot is one method of reducing risk of impacts.

4.3 Future Work

There are numerous areas for research and improvement of the linear SEAs. It is imperative to validate the performance of the actuators to compare them with similar ball screw driven actuator designs. A custom actuator test stand has been developed which supports a multitude of experimental setups with the actuators and joint assemblies representative of the joints on THOR. This test stand enables testing of custom controllers prior to use on the robot. Through the use of digital image correlation (DIC) to track the movement of actuator components under load, advanced measurements can be taken to analyze stresses within the actuator structure, backlash between the universal joints, actual deflection paths of the

compliant beam, and the effective stiffnesses of the Hoeken's linkage and other components typically assumed to be rigid.

Furthermore, a new kinematic model of ball screw driven SEAs has been developed which more accurately describes the actuator dynamics, and has been validated on the actuator test stand [61]. This new model provides a means of accurately simulating the performance of new actuator designs, and will enhance understanding of the principles and limitations of linear SEAs. Similarly, an analogous version of the model can and should be applied to rotary actuators and can be validated on the modular actuator test stand.

There are numerous control strategies for SEAs which can be developed and tuned for the THOR actuators. The impedance controller currently used on THOR relies on a disturbance observer to counteract the effects of unmodeled disturbances and friction. The addition of an adaptive friction compensator could greatly improve the sensitivity and resolution of commandable forces. Lastly, there are other linear SEA applications to explore aside from humanoids. One such use would be to use two actuators in a parallel arrangement to create a low-profile two-DOF assistive boot or prosthesis.

Series elastic actuator design and performance have come a long way since their inception decades ago. As bipedal locomotion strategies continue to improve, the demand for more lightweight, powerful, sensor-dense actuators will increase. Safe actuation with force sensing and compliance will be imperative to humanoid robots integrating into human-centered environments and performing tasks in close proximity to humans. By researching innovative design and control strategies, knowledge of the advantages and disadvantages of various approaches can be applied to future SEA designs.

Bibliography

[1] G. Pratt and M. Williamson, "Series Elastic Actuators," in *IEEE/RSJ International Conference on Intelligent Robots and Systems. Human Robot Interaction and Cooperative Robots*, vol. 1. IEEE Comput. Soc. Press, 1995, pp. 399–406.

[2] J. E. Pratt and B. T. Krupp, "Series Elastic Actuators for Legged Robots," *Proceedings of SPIE*, vol. 5422, pp. 135–144, Sep. 2004.

[3] J. Pratt, B. Krupp, and C. Morse, "Series Elastic Actuators for High Fidelity Force Control," *Industrial Robot: An International Journal*, vol. 29, no. 3, pp. 234–241, 2002.

[4] D. W. Robinson, J. E. Pratt, D. J. Paluska, and G. A. Pratt, "Series Elastic Actuator Development for a Biomimetic Walking Robot," in *IEEE/ASME International Conference on Advanced Intelligent Mechatronics*, 1999.

[5] D. Paluska and H. Herr, "The effect of series elasticity on actuator power and work autput: Implications for robotic and prosthetic joint design," *Robotics and Autonomous Systems*, vol. 54, no. 8, pp. 667 – 673, 2006.

[6] N. Paine, S. Oh, and L. Sentis, "Design and Control Considerations for High Performance Series Elastic Actuators," *IEEE/ASME Transactions on Mechatronics*, vol. PP, no. 99, pp. 1–12, 2013.

[7] J. W. Hurst, A. A. Rizzi, and D. Hobbelen, "Series Elastic Actuation: Potential and Pitfalls," in *International Conference on Climbing and Walking Robots*, 2004.

[8] D. Lahr, V. Orekhov, B. Lee, and D. Hong, "Development of a Parallely Actuated Humanoid, SAFFiR," in *Proceedings of the ASME International Design Engineering Technical Conference*, 2013.

[9] B. Lee, C. Knabe, V. Orekhov, and D. Hong, "Design of a Human-Like Range of Motion Hip Joint for Humanoid Robots," in *Proceedings of the ASME International Design Engineering Technical Conference*, 2014.

[10] G. Pratt, "Low Impedance Walking Robots," *Integrative and Comparative Biology*, vol. 181, pp. 174–181, 2002.

[11] J. Pratt and B. Krupp, "Design of a Bipedal Walking Robot," in *Proceedings of SPIE*, G. R. Gerhart, D. W. Gage, and C. M. Shoemaker, Eds., vol. 6962, no. 2008, Apr. 2008, pp. 69 621F–1–69 621F–13.

[12] K. Kong, J. Bae, and M. Tomizuka, "A Compact Rotary Series Elastic Actuator for Human Assistive Systems," *IEEE/ASME Transactions on Mechatronics*, vol. 17, no. 2, pp. 288–297, 2012.

[13] D. Accoto, G. Carpino, F. Sergi, N. Luigi, L. Zollo, and E. Guglielmelli, "Design and Characterization of a Novel High-Power Series Elastic Actuator for a Lower Limb Robotic Orthosis," *International Journal of Advanced Robotic Systems*, vol. 10, no. 359, pp. 1–12, 2013.

[14] C. M.-w. Eddie, "Rotary Elastic Actuator," Master's thesis, National University of Singapore, 2004.

[15] B. Lee, D. Lahr, V. Orekhov, and D. Hong, "Design and Measurement Error Analysis of a Low-Friction Lightweight Linear SEA," in *Proceedings of the ASME 2013 International Design Engineering Technical Conferences & Computers and Information in Engineering Conference*, 2013, pp. 1–8.

[16] C. Knabe, B. Lee, V. Orekhov, and D. Hong, "Design of a Compact, Lightweight, Electromechanical Linear Series Elastic Actuator," in *Proceedings of the ASME International Design Engineering Technical Conference*. Virginia Tech, 2014.

[17] S. A. Migliore, E. A. Brown, and S. P. Deweerth, "Biologically Inspired Joint Stiffness Control," in *Proceedings of the 2005 IEEE International Conference on Robotics and Automation*, no. April. Georgia Institute of Technology, 2005, pp. 4508–4513.

[18] J. Hurst, J. Chestnutt, and A. Rizzi, "The Actuator with Mechanically Adjustable Series Compliance," *IEEE Transactions on Robotics*, vol. 26, no. 4, pp. 597–606, 2010.

[19] B. Vanderborght, A. Albu-Schaeffer *et al.*, "Variable Impedance Actuators: A Review," *Robotics and Autonomous Systems*, vol. 61, no. 12, pp. 1601–1614, Dec. 2013.

[20] S. Wolf and G. Hirzinger, "A New Variable Stiffness Design: Matching Requirements of the Next Robot Generation," in *2008 IEEE International Conference on Robotics and Automation*. Institute of Robotics and Mechatronics, 2008, pp. 1741–1746.

[21] C.-m. Chew, G.-s. Hong, and W. Zhou, "Series Damper Actuator: A Novel Force/Torque Control Actuator," in *IEEE International Conference on Humanoid Robots*, 2004, pp. 533–546.

[22] M. Laffranchi, N. Tsagarakis, and D. Caldwell, "A Compact Compliant Actuator (CompAct$^{\text{TM}}$) with Variable Physical Damping," in *2011 IEEE International Conference on Robotics and Automation*, Shanghai, China, 2011, pp. 4644–4650.

[23] K. Kong, J. Bae, and M. Tomizuka, "Control of Rotary Series Elastic Actuator for Ideal Force-Mode Actuation in Human–Robot Interaction Applications," *IEEE/ASME Transactions on Mechatronics*, vol. 14, no. 1, pp. 105–118, 2009.

[24] L. Amaral, B. Jardim, and A. Siqueira, "Robust Force and Impedance Control of Series Elastic Actuators," in *ABCM Symposium Series in Mechatronics*, vol. 5, 1994, pp. 212–221.

[25] H. Vallery, R. Ekkelenkamp, H. van der Kooij, and M. Buss, "Passive and accurate torque control of series elastic actuators," in *IEEE/RSJ International Conference on Intelligent Robots and Systems*. Ieee, Oct. 2007, pp. 3534–3538.

[26] V. Orekhov, D. Lahr, B. Lee, and D. Hong, "Configurable Compliance for Series Elastic Actuators," in *Proceedings of the ASME 2013 International Design Engineering Technical Conferences and Computers and Information in Engineering Conference*, 2013, pp. 1–8.

[27] R. Van Ham, T. Sugar, B. Vanderborght, and K. Hollander, "Compliant Actuator Designs," *IEEE Robotics and Automation magazine*, pp. 81–94, Sep. 2009.

[28] D. Lahr, "Design and Control of a Bipedal Robot," Ph.D. dissertation, Virginia Polytechnic Institute and State University, 2014.

[29] B. Lee, "Design of a Humanoid Robot for Disaster Response Design of a Humanoid Robot for Disaster Response," Master's thesis, Virginia Polytechnic Institute and State University, 2014.

[30] D. W. Robinson and G. A. Pratt, "Force Controllable Hydro-Elastic Actuator," in *IEEE/ASME International Conference on Robotics and Automation*, 2000.

[31] G. Bilodeau and E. Papadopoulos, "Development of a Hydraulic Manipulator Servoactuator Model: Simulation and Experimental Validation," in *Proceedings of the IEE International Conference on Robotics and Automation*, 1997, pp. 1547–1552.

[32] S. Ates, V. Sluiter, P. Lammertse, and A. Stienen, "ServoSEA Concept: Cheap, Miniature Series-Elastic Actuators for Orthotic, Prosthetic and Robotic Hands," in *IEEE RAS & EMBS International Conference on Biomedical Robotics and Biomechatronics (BioRob)*, 2014, pp. 752–757.

[33] L. Martins, R. Pretto, R. Gerndt, and R. Guerra, "Design of a Modular Series Elastic Upgrade to a Robotics Actuator," in *Proceedings of the 18th Annual RoboCup International Symposium*, 2014.

[34] N. Paine, "High-Performance Series Elastic Actuation," Ph.D. dissertation, The University of Texas at Austin, 2014.

[35] M. Taylor, "A Compact Series Elastic Actuator for Bipedal Robots with Human-Like Dynamic Performance," Master's thesis, Carnegie Mellon University, 2011.

[36] J. W. Sensinger and R. F. Weir, "Improvements to Series Elastic Actuators," in *IEEE/ASME International Conference on Mechatronic and Embedded Systems and Applications*, 2006, pp. 1–7.

[37] A. Edsinger-Gonzales and J. Weber, "Domo: A Force Sensing Humanoid Robot for Manipulation Research," in *IEEE International Conference on Humanoid Robots*, 2004, pp. 273–291.

[38] M. Slovich, N. Paine, K. Kemper, A. Metger, A. Edinger, J. Weber, and L. Sentis, "Building HUME: A Bipedal Robot for Human-Centered Hyper-Agility," *Dynamic Walking*, 2012.

[39] P. Gregorio, M. Ahmadi, and M. Buehler, "Design, Control, and Energetics of an Electrically Actuated Legged Robot," *IEEE Transactions on Systems, Man, and Cybernetics*, vol. 27, no. 4, pp. 626–634, 1997.

[40] J. Pratt and P. G, "Intuitive Control of a Planar Bipedal Walking Robot," in *IEEE International Conference on Robotics and Automation*, 1998, pp. 2014–2021.

[41] K. W. Hollander, R. Ilg, T. G. Sugar, and D. Herring, "An Efficient Robotic Tendon for Gait Assistance." *Journal of biomechanical engineering*, vol. 128, no. 5, pp. 788–91, Oct. 2006.

[42] K. W. Hollander and T. G. Sugar, "Design of Lightweight Lead Screw Actuators for Wearable Robotic Applications," *Journal of Mechanical Design*, vol. 128, no. 3, pp. 644–648, 2006.

[43] K. W. Hollander, T. G. Sugar, and D. E. Herring, "Adjustable Robotic Tendon using a 'Jack Spring'™," in *IEEE International Conference on Rehabilitation Robotics*, 2005, pp. 113–118.

[44] T. Morita and S. Sugano, "Design and Development of a new Robot Joint using a Mechanical Impedance Adjuster," in *IEEE International Conference on Robotics and Automation*, 1995, pp. 2469–2475.

[45] A. Tasch, "A Two-DOF Manipulator with Adjustable Compliance Capabilities and Comparison with the Human Finger," *Journal of Robotic Systems*, vol. 13, no. 1, pp. 25–34, 1996.

[46] S. Kawamur, T. Yamamoto, D. Ishida, T. Ogata, Y. Nakayama, and S. Sugiy, "Development of Passive Elements with Variable Mechanical Impedance for Wearable Robots," in *Proceedings of the IEEE International Conference on Robotics and Automation*, no. May, 2002, pp. 248–253.

[47] R. Wang and H. Huang, "AVSER — Active Variable Stiffness Exoskeleton Robot System: Design and Application for Safe Active-Passive Elbow Rehabilitation," *2012 IEEE/ASME International Conference on Advanced Intelligent Mechatronics (AIM)*, pp. 220–225, Jul. 2012.

[48] J. Choi, S. Hong, W. Lee, S. Kang, and M. Kim, "A Robot Joint With Variable Stiffness Using Leaf Springs," *IEEE Transactions on Robotics*, vol. 27, no. 2, pp. 229–238, 2011.

[49] S. Ressler, "Design and Implementation of a Dual Axis Motor Controller for Parallel and Serial Series Elastic Actuators," Master's thesis, Virginia Polytechnic Institute and State University, 2014.

[50] R. L. Norton, "Design of machinery," pp. 140–145, 2008.

[51] R. Norton, "In Search of the 'Perfect' Straight Line and Constant Velocity Too," in *Proceedings of the 6th Applied Mechanisms and Robotics Conference*, 1999.

[52] R. R. Bulatović and S. R. Dordević, "On the Optimum Synthesis of a Four-Bar Linkage Using Differential Evolution and Method of Variable Controlled Deviations," *Mechanism and Machine Theory*, vol. 44, no. 1, pp. 235–246, Jan. 2009.

[53] J. Breen and M. Hayner, "Actuator including mechanism for converting rotary motion to linear motion," Sep. 29 2011, uS Patent App. 12/732,321.

[54] F. Barlas, "Design of a Mars Rover Suspension Mechanism," Master's thesis, Izmir Institute of Technology, 2004.

[55] A. Rodriguez and M. T. Mason, "Effector Form Design for 1DOF Planar Actuation," in *2013 IEEE International Conference on Robotics and Automation*. Ieee, May 2013, pp. 349–356.

[56] S. Lu, D. Zlatanov, X. Ding, and R. Molfino, "A New Family of Deployable Mechanisms Based on the Hoeken's Linkage," *Mechanism and Machine Theory*, vol. 73, no. October 2012, pp. 130–153, Mar. 2014.

[57] L. Barb, O. Piccin, J. Gangloff, B. Bayle, and R. Rump, "Design of a Linear Haptic Display Based on Approximate Straight Line Mechanisms," in *IEEE International Conference on Intelligent Robots and Systems*, Teipei, Taiwan, 2010, pp. 5048–5053.

[58] S. K. Saha, R. Prasad, and A. K. Mandal, "Use of Hoeken's and Pantograph Mechanisms for Carpet Scrapping Operations," in *Proc. of the 11th Nat. Conf. on Machines and Mechanisms*, 2003, pp. 732–738.

[59] B. Fremgen, "Atrophy-Reducing Movable Foot Support Apparatus," p. 14, 2011.

[60] J. Beroz, S. Awtar, and A. J. Hart, "Extensible-Link Kinematic Model For Determining Motion Characteristics of Compliant Mechanisms," in *Proceedings of the ASME International Design Engineering Technical Conference*, 2013, pp. 1–9.

[61] V. Orekhov, C. Knabe, M. Hopkins, and D. Hong, "An Unlumped Model for Linear Series Elastic Actuators with Ball Screw Drives," in *Submitted to IEEE International Conference on Robotics and Automation*, 2015.